Computational aspects of generalized continua based on moving least square approximations

Sebastian Skatulla

Thesis submitted to the University of Adelaide
for the degree of Doctor of Philosophy

September, 2006

School of Mechanical Engineering
The University of Adelaide

Chapter 1

Introduction

1.1 Background

In modern physics it is a well-known fact that matter on the microscopic scale is discontinuous as one can distinguish molecules, atoms and even smaller units. Traditional engineering however, is usually concerned with problems which are related to a significantly larger scale than the one which the construction elements of matter belong to. Therefore, the classical continuum theory assumes that with the exception of discontinuity surfaces all mechanical fields smoothly vary over the spatial dimensions of the continuum, such that higher gradients or degrees of freedom beyond displacements are negligible. In this context the variation of strain is considered to be substantial only within a so-called *representative volume element* (RVE) to which the external loading corresponds. As a result elastic moduli can be found which represent the material behaviour of the entire body. In this sense elastic material properties are always associated with the RVE and are a statistical average. Consequently, these properties can be applied to field equations which describe the behaviour of a body in the limit. The concept though, is based on the presumption that the RVE is large enough compared to the size of the micro-constituents such as granule, crystalline or heterogeneous aggregates, so that the behaviour of the single constituent and the interaction to each other can be neglected. It also implies that a large number of micro-constituents respond to an external stimuli as a whole and mean values of material properties can be taken which represent the entire body. Thus, the validity of the classical field theory has to be questioned especially for small-scale structures, where the external loading interrelates to sub-continua which refer to the micro-constituents. That is, the dimensions of the body under consideration are not very much greater than the characteristic length of the material of this body, e.g. interatomic spacing in a crystal or the particle size of a granular material. In this case no statistical average can be found which can be applied to field equations valid for the whole body. Consequently, strategies have to be considered which go beyond the classical continuum approach and lead to new enriched theories.

A large number of phenomenological constitutive models have been proposed in the last two decades which captured macroscopic material behaviour found by empirical observation

within the mechanics of metal, polymer, concrete, wood as well as geo- and bio-materials. In opposition to phenomenological methods, predictive models rely on a thorough analysis of a material's micro-structure as well as the understanding of the microscopic processes which lead to a certain macroscopic response such as plastic hardening induced by dislocation within a crystal lattice (Fleck *et al.* 1994), microcrack induced creep or embrittlement due to stress corrosion. Moreover, it must be distinguished between microscopic processes related to the atomic or molecular scale as well as material behaviour which originates at the micro-structure of some sub-macroscopic scale, e.g. ductile fracture characterized by void nucleation, growth and coalescence (Garrison and Moody 1987), sintering material due to a decreasing porosity or a particular kind of creep damage caused by an increasing number of micro-cracks along grain boundaries. One way to account for these kind of phenomena was to incorporate internal variables which address the void nucleation or the density of micro-cracks as well as the scaling ratio of micro- to macro-space (e.g. Gurson 1977; Rousselier 1987; Tvergaard and Needleman 1995; Sun *et al.* 1997).

Alternatively, non-classical continuum mechanical formulation can be considered which involve specially designed kinematical quantities, stress measures or internal variables and their dependency on position and time. Furthermore, the purely mechanical approach could also be extended to include interaction with thermal or chemical factors which can be found for degrading bodies, as well as other physical phenomena such as electrical-mechanical coupling. These generalized continuum formulations were already shown to be able to address orientation of a material as well as micro-structural effects which lead to localization of deformation, e.g. the development of shear bands (e.g. Triantafyllidis and Aifantis 1986; Gutkin and Aifantis 1999).

The development of generalized continuum theories can be traced back to early foundations that have been laid by researchers like Cauchy (1850), Voigt (1887) and the Cosserat brothers (1909). The motivation was to extend the physical range of the validity of continuum methods. At the end of the fifties, major input came Ericksen and Truesdell (1957) who provided a differential description of an oriented body. Each material point was associated with an additional set of directors which were functions of the conventional deformation gradient tensor. These directors could deform in the sense of stretch and rotation and allowed to formulate the so-called Wryness tensor. Also, the milestone work of the brothers Cosserat was translated into modern tensor notation (Günther 1958; Schäfer 1967). Subsequently, geometrically linear formulations were proposed involving non-linear material behaviour such as plasticity (Lippmann 1969; Besdo 1974). A further development and generalization was to consider the directors as a micro-displacement gradient tensor independent of the macro-displacement and to define a relative deformation gradient between macro- and micro-continuum (Mindlin 1964). Additionally, a second order gradient tensor was introduced which was the macro-gradient of the micro-displacement gradient. The incorporation of these two non-classical gradient tensors into the classical potential energy density required five extra linear elastic parameters. It was also mentioned that it would be possible to integrate the size of the micro-continuum into the constitutive parameters. Moreover, it was shown that the classical couple stress theories (Toupin 1962; Koiter 1964) were encompassed as special cases. Classical couple stress theories commonly involve only one additional material parameter and do actually not regard any microstructure. Taking up again the idea

of micro-directors attached to each material point, it is possible to constrain the motion of these directors in such a way that the micro-body only exhibits certain strain conditions. In this sense the continuum is called micromorph, if the micro-body undergoes stretch, shear and rigid body rotations, microstretch for stretch and rigid body rotation only and micropolar, if the micro-continuum behaves as a rigid body (Eringen and Suhubi 1964; Eringen and Kafadar 1976; Eringen 1999). Micropolar continuum mechanical models originated in the so-called *Cosserat* theory of elasticity (Cosserat and Cosserat 1909) are characterized by the property that each material point inherits a rotation field which is independent of and additional to the conventional displacement field. The material response of a body to an external stimuli is a corresponding force stress field (force per unit area) as well as a couple stress field (torque per unit area). Whereas the classical elasticity involves two elastic constants, isotropic micropolar elastic solids account for at least one extra material constant. These additional elastic constants corresponding to the couple stress are dependent on a so-called characteristic length scale parameter which can be related to the material's micro-structure.

Classical elasticity does not account for contributions of strain gradients which can be linked to the micro-structure with physical properties such as compactness of the packing, particle size, crystal lattice structure or contact friction between the particles (Aifantis 1999). This can lead to an underestimation of the magnitude of the stresses, but also of their distribution. To the contrary, generalized continua can be designed to incorporate material information from the microscopic space into a macroscopic constitutive model. Triantafyllidis and Aifantis (1986) demonstrated that for localized deformation of hyperelastic materials, the tendency of the resulting governing equations to lose ellipticity can be overcome by incorporating second order gradient of the deformation field into the stored energy function. Furthermore, this approach provided a natural way not only to predict direction and the critical stress levels, but also the size of the localized zone can be controlled by an additional material parameter.

The need of alternative generalized continuum formulations was also recognized, when so-called size-scale effects have been observed for problems which were characterized by a critical ratio of macro- to micro-geometry. This was found e.g. for elastic bending experiments of marble (Vardoulakis *et al.* 1998) and epoxy polymeric beams (Lam *et al.* 2003). Also in porous media, such as bone or foam material, similar size-scale effects were noticed for pore diameters significant compared to the specimen size (Yang and Lakes 1981; Lakes 1986; Aifantis 1999). In all cases classical theories substantially failed to predict the experimental results. In contrast, the *Cosserat* theory applied by Lakes and his co-workers as well as the strain gradient theory developed by Aifantis and his colleagues were shown to approximate the experimental data very well. In the approach of Aifantis and his co-workers Hook's law was modified to incorporate strain gradients up to second order and additional material constants were associated with the first as well as the second order strain gradients. The idea was motivated by the approximation of the average strain by a Taylor expansion, where only terms up to second order were maintained (Mühlhaus and Aifantis 1991). The additional material constants were necessary to calibrate the formulation to different kinds of problems and materials.

The ability to describe orientation and size of the material constituting particles in a

completely natural way predestined micropolar continua in particular, to predict physical phenomena which are related to the microstructure. An example was the modelling of size effects in crystal plasticity (Forest *et al.* 2000). In the domain of non-linear material behaviour, linear micropolar continuum theories have especially been accounted for in simulating of strain localization phenomena within plasticity. In particular, it was discovered that the loss of ellipticity of the underlying governing equations and the pathological mesh dependency of finite element solutions could be overcome by micropolar continuum based formulations (Mühlhaus and Vardoulakis 1987; Mühlhaus 1989; de Borst 1993). The next logical step was to formulate non-linear micropolar continuum theories in the sense of a geometrically exact description of finite deformation and rotation (Sansour and Bufler 1992; Sievert 1992; Steinmann 1994; Sansour and Bednarczyk 1995; Sansour 1998a).

Another way to deal with heterogeneous materials was to establish a relation between a macro- and meso- or micro-domain in terms of localization and homogenization techniques (Aboudi 1999, Williams 2005). That was for an example to compute the micro-strain by localizing the macro-strain so that the constitutive law could be applied on the micro-space calculating the micro-stress. Subsequently, the micro-stress was projected by a homogenization rule onto the macro-space again (Forest 1998). It was shown that the homogenization could also be achieved by making use of internal variables such as the fluctuation of kinematical quantities which cause energy dissipation within the meso-continuum. The material law was therefore defined on the meso-scale incorporating those internal variables (Walsh and Tordesillas 2004).

When it comes to modelling formulations of solids and structures, it is the finite element method (FEM) which is the usual choice. However, in case of formulations which involve higher order derivatives such as strain gradient plasticity theory, it was shown that their implementation into the finite element code is rather limited. In the one- and two-dimensional case cubic Hermite type shape-functions are able to provide C^1 continuity, because they interpolate the displacement field as well as their first derivatives. The performance of these type of elements however, was reported to be poor in the context of strain gradient theories (Xia and Hutchinson 1996), and the extension to a three-dimensional interpolation is considered to be too complex. Another way of dealing with higher order derivatives proposed by Xia and Hutchinson was to utilize hybrid elements interpolating displacement, the first order derivatives of the displacement and the anti-symmetric component of the stresses. An approach, which went one step further, was to incorporate not only strain and first order strain gradient but also the second order strain gradient. In order to confine the number of nodal degrees of freedom the use of C^1 continuous elements was proposed so that only the first and second order derivatives of the displacement had to be approximated (Zervos *et al.* 2001). The result was in either case a very large number of nodal degrees of freedom.

Contrarily, so-called *meshfree methods* based on moving least squares (MLS) can easily provide higher order continuity and are considered in this work to be the logical alternative to FEM. It was only within the last decade that the research activity into meshfree methods significantly increased, realizing that these methods can deal especially well with problems characterized by extensive deformations, changing domain geometry, or necessitate higher order approximation continuity. These are areas, where the more established finite

element method (FEM) exhibits shortcomings. Essentially, meshfree methods do not require a rigid background mesh which is beneficial as finite element modelling of large deformation problems usually leads to mesh distortion which makes re-meshing necessary. In most large-scale numerical simulations of physical phenomena however, a high percentage of the overall computational effort is expended on technical details connected with meshing. These details include, in particular, grid generation, mesh adaptation to domain geometry, element or cell connectivity, grid motion, and separation of mesh cells to model fracture, fragmentation and free surfaces. Moreover, in most computer-aided design work, the generation of an appropriate mesh constitutes, by far, the most costly portion of the computational analysis.

In order to solve problems given as partial differential equations (PDE) computationally, the PDE must be approximated and discretized. Within meshfree methods, two different methodologies can be found in literature to achieve this: Firstly, there are methods dealing with the strong form of the PDE. An example of these is the *smoothed particle hydrodynamics* (SPH) method developed by Lucy, Gingold and Moghan in the early stages of meshfree methods in the 1970s (Lucy 1977; Gingold and Monaghan 1977; Monaghan 1985). Originally, this method was applied to simulate problems without boundaries such as exploding stars and dust clouds in astrophysics. Later, other authors modified SPH so that, because of its efficiency, it also became popular in other research fields such as molecular dynamics and hydromechanics. However, the strong form of the PDE is not commonly used. Generally, the Galerkin weak formulations is preferred, because no higher order derivatives are involved. The various Galerkin weak formulations are the second kind of methods that are mainly applied to solve PDEs. These methods have been commonly called *meshfree Galerkin methods* and became popular at the beginning of the 1990s. In this context SPH was applied to problems involving a material law, but it became obvious that the exactness of the solution was not sufficient (see e.g. Belytschko et *al.* 1996). A known reason for this is the fact that the used approximants are similar to the Shepard-approximants (Shepard 1968), which have been shown to provide insufficient solution accuracy (see e.g. Duarte and Oden 1996). Groups of researchers in France (Nayroles, Breitkopf, Touzot, Villon) as well as the USA (Belytschko and Liu), were therefore looking for new strategies to make meshfree methods applicable in solid mechanics. By this, in 1992 the french group re-discovered the *moving least square method*, formerly derived by Shepard (Shepard 1968) and further improved by Lancaster and Salkauskas (Lancaster and Salkauskas 1981). This discovery subsequently was the starting point of a quickly growing interest in meshfree methods and of their rapid development within the last fifteen years.

A brief literature on meshfree methods will familiarize the reader with most important developments since their introduction.

- **Diffuse element method (DEM)**

  After the French group had re-discovered MLS they made it usable for engineering computations and presented their *diffuse element method* (Nayroles, Touzot and Villon 1992; Breitkopf, Touzot and Villon 1998; Breitkopf *et al.* 2000). In their first approach the authors simplified the derivation of the approximated solution function. That is, it was only partially derived, because they considered the coefficients of the basis polynomial,

used for approximation of the solution function in Galerkin methods, as constant in the vicinity of the sample points which are the particles.

From an implementational point of view DEM is similar to the *element free Galerkin method* and the *reproducing kernel particle method* described in the next paragraph. However, it was recognized by Nayroles and his co-workers that the precision and the convergence rate was quite poor in comparison to FEM and to other meshfree methods using complete approximation derivatives.

In general, they stated that the reason for the lesser convergence of all meshfree methods based on MLS was the rational (non-polynomial) shape of the MLS-approximants opposed to the FEM ones (Breitkopf et. al. 2002). However, the commonly applied Gauss-Legendre integration scheme would require shape functions with polynomial form for high convergence rates. Therefore, they introduced a special adaptive integration scheme, where the original integration weights were modified. This procedure involved the solving of an equation system that incorporated integration constraints that were to be fulfilled for proper exactness. Although high solution precision was reached, this equation system must be solved in each integration cell. For this reason the researchers themselves found fault with the computational costs.

- **Element free Galerkin method (EFGM) and the reproducing kernel particle method (RKPM)**

  The *element free Galerkin method* developed by Belytschko and his co-workers (Belyschko *et al.* 1994b; Belyschko *et al.* 1996; Belytschko *et al.* 2000) and the *reproducing kernel particle method* introduced by Liu and his co-workers (Liu *et al.* 1996; Li and Liu 1998; Li and Liu 2000) are quite alike. Both methods can be traced to the MLS-algorithm, where RKPM though, can be seen as an advanced version of it. The main difference between both is that in EFGM a discrete approach was chosen, whereas in RKPM it was started from a continuous one, where the interpolation functions had to be integrated. The implementational details of both methods however, are practically equivalent.

  The discrete version of RKPM exhibits subtle differences to MLS, such as the shifted basis and a variable support of the approximants (Gosz and Liu 1996; Jun *et al.* 1998). The original splines were modified regarding the particle support which was defined by a dilation parameter and the lumped particle weight. The dilation parameter was a constant which could be calculated by using the energy error ratio from a normalized set of particles. A shifted basis meant that the polynomial was centered by the usage of local coordinates. The local coordinates were expressed as the ratio of the distance of the sample points to the evaluation points and the influence radius of the sample points, the particles.

  As it comes to the imposition of the essential boundary conditions Belytschko and his co-workers applied the penalty method (Belytschko *et al.* 1994a), the Lagrange multiplier method (Belytschko *et al.* 1994b; Dolbow and Belytschko 1998), modified variational principles (Lu *et al.* 1994), or a combination with finite elements (Krongauz and Belytschko 1996). Liu and his co-worker developed a special algorithm based on a traditional collocation method which resulted in modified RKPM shape functions which possessed at boundary the *Kronecker Delta property* (Wagner and Liu 2000).

The continuity of the EFGM- and the RKPM-appproximants was not only dependent on the basis polynomial, but was further improved by usage of splines. Furthermore, the authors claimed that at the boundary a high solution accuracy could be achieved. However, this can not fully be confirmed, as double curved surfaces especially, lead to reduced approximation accuracy. Another difficulty is the determination of the particle supports or zones of influence. These had to be varied in both methods to find out the optimal influence radius for each particle. That is, it must be ensured that a minimum number of particles support each point of the domain, otherwise the computation is not stable. Especially for irregular particle distributions, this is a tricky task. This fact was also emphasized by Liu and his co-workers (Chen *et al.* 1996). In addition, it was realized that the computation of the approximants and the numerical integration of the final discrete equation system consumes considerably more computer performance than FEM. A main reason for the performance difference is the essentially greater support of the particles in meshfree methods.

- **hp-cloud method**

  Duarte and Oden proposed a meshfree method called the *hp-cloud method* (Duarte and Oden 1996; Liszka *et al.* 1996) in which they modified Shepard- or MLS-approximants by multiplication with higher order basis functions such as Legendre polynomials. One could consider this modification is a kind of enrichment which however, increases the necessary computational costs to generate these shape functions. On the other hand, because the Shepard shape functions were preferred, this drawback may be levelled out. This means in particular that the approximation performance of the enriched Shepard functions was improved. The characters h and p denote that his method and the meshfree approximation, respectively, should be flexible in the sense of h-adaptivity and p-adaptivity. The authors expounded that the resulting approximants satisfied the *partition of unity* property at any point of the domain. Similar to Liu and his co-workers, they showed that non-polynomial functions, e.g. trigonometric functions, might also be incorporated.

  Lagrange multipliers were chosen to impose Dirichlet boundary conditions. Furthermore, a second method has been analyzed to handle the boundary condition. They denoted it as boundary projection which was originally based on theories of Lancaster and Salkauskas (1981).

  For the integration of the problem formulation Duarte, as well as Liu and Belytschko, suggested a Gauss-Legendre quadrature.

- **Partition of unity method**

  Melenk and Babuska (1997) concentrated their research efforts on developing the *partition of unity method* which went in a similar direction as Duarte, but in a more general way. They also chose approximation function - mainly simple ones - which fulfill the partition of unity condition and multiplied them with a suitable basis of linear independent functions. The term 'suitable' means that, based on the knowledge of the behaviour of the solution function, an adequate basis should be selected which would be able to reproduce this function sufficiently accurate.

- **Natural neighbour Galerkin method**

  Sukumar *et al.* (2001) developed a meshfree method, the so-called natural neighbour Galerkin method, which is originated in the natural element method (NEM) (Traversoni, 1994; Braun and Sambridge 1995; Sukumar, Moran and Belytschko 1998). This meshfree method aimed to combine the advantages of FEM and the known meshless methods, but without their disadvantages.

  The approximation of an unknown field function is constructed using a *Voronoi diagram* together with a *Delaunay tesselation*. These geometrical methods had three objectives: Firstly, to obtain a irregular distribution of nodes, secondly, the so-called *influence zones* of these nodes and thirdly the overlapping of adjacent nodes. Afterwards the entire domain was subdivided into polygons which were used to apply the Gaussian quadrature. The Voronoi diagram and the Delaunay tesselation were not only used for the numerical integration, but also to construct the test and trial functions. Hereby, the authors made use of the so-called non-Sibsonian interpolation scheme (Belikov et al. 1997) which was referred to the natural neighbour co-ordinates, introduced by Sibson (1980). They demonstrated that their method was capable of enforcing the essential boundary conditions as easily as in FEM, because the non-Sibsonian approximants maintained the *Kronecker Delta condition* at the particles. Furthermore, they showed that the non-Sibsonian approximants fulfilled the *partition of unity* condition and possessed at least C^1 consistency everywhere.

  The presented algorithm to calculate the non-Sibsonian shape functions in $\mathbb{R}^3$ is however quite involved and also the set-up of the *Voronoi diagram* and the *Delaunay tesselation* is not an easy task in the three-dimensional space.

- **Meshless local Petrov-Galerkin method (MLPG) and local boundary integral equation method (LBIE)**

  As truly meshless methods Alturi and Zhu introduced the *meshless local Petrov-Galerkin method* (Atluri and Zhu 1998; Atluri and Zhu 2000a) and the *local boundary integral equation method* (Atluri and Zhu 2000b; Zhu, 1999; Zhu, Zhang and Atluri 1999). One main difference between both methods was the different usage of test and trial functions. The MLPG method belongs to the *Petrov-Galerkin*-family for which two unequal function spaces are characteristic. On the other hand the LBIE theory belongs to the conventional *Bubnov-Galerkin* methods. In MLPG as well as in LBIE the approximation of the trial functions was achieved by MLS-approximants.

  Now, the following properties are similar for both methods. The assembly of the global discrete equation set was achieved without underlaying shadow FEM elements. This laid in the fact that Alturi and Zhu applied the weak form of the PDE separately to each particle support. Correspondingly, the numerical integration of these local PDEs was performed independently within each particle support. One achieves for each computed support patch as a result one equation and so, a global equation system can be assembled containing as many lines as necessary to obtain all the global unknowns.

  For integration purposes, Alturi and Zhu chose a *Gauss-Legendre quadrature* on each of the regularly distributed particle patches. However, the computation of the Gauss coordinates

and weights was unspecified. A drawback may be that, because of the overlapping of all particle sub-domains, the integration costs are probably higher than applying a global problem formulation onto the underlying background mesh.

- **Finite spheres method**

  De and Bathe presented a meshfree method which they called *finite spheres method* (De and Bathe 2000; De and Bathe 2001). As shape functions they chose *Shepard* approximants so that the partition of unity condition was fulfilled. The authors stated that the computational performance was not as high as in the recent FEM. Furthermore, if only the displacement function was interpolated, volumetric locking appeared. Therefore they proposed a mixed formulation involving the approximation of displacement and pressure.

  As well as Breitkopf *et al.* (2002), they elaborated that the *Gauss-Legendre* integration scheme was not suitable by means of exactness considering the non-polynomial form of their meshfree approximants. Due to this characteristic the authors proposed to replace the commonly utilized *Gauss-Legendre* with the *Gauss-Chebyshev* integration scheme. However, the needed amount of integration points were much larger than applying *Gauss-Legendre* quadrature. Above all, it was necessary to treat the boundary areas in a special manner - they denoted it as *integration on a lens*. Therefore, even if a higher solution accuracy could be achieved, it involved extra computational efforts.

- **Local maximum entropy approximation schemes**

  The local maximum entropy approximation schemes proposed by (Arroyo and Ortiz 2006) is a new and interesting approach to achieve a meshfree approximation. Its computation is constrained by the partition of unity condition as well as the first order consistency conditions and the positivity of the shape functions, where the latter leads to a so-called *convex approximation*. The domain is discretized by a *Delaunay triangulation*, where the Delaunay approximants are computed in a sense that they maximize the so-called approximation entropy. The *maximum entropy principle* is well-known in the information theory and statistical physics, where probability schemes are evaluated by means of minimizing the certainty of known events and maximizing the uncertainty of unknown events. This principle clearly exhibits an analogy to the least square method considering as known events a set of sample points of a certain function which need to be approximated. Since the *maximum entropy principle* is non-local, additionally a locality requirement needs to be enforced by introducing a weight function and formulating a minimization problem which needs to be solved iteratively e.g. applying the *Newton Raphson method*. The approximants satisfy the weak *Kronecker Delta* property which is clearly of great benefit imposing essential boundary conditions. However, considering that the presented examples are characterized by simple geometries, it is not quite clear, if this weak *Kronecker Delta* property is sufficient for more complex structures. An open issue is the extension of this approximation scheme so that higher order continuity can be achieved.

The high diversity of meshfree methods clearly indicates the intense research undertaken in this area as well as their current popularity. Even if their use in real engineering problems is not as wide-spread yet, they already have been applied to mechanical engineering problems in the form of case studies in metal forming (Xiong et. al. 2005), dynamic fracture

(Belytschko and Tabbara 1996) and shear band propagation (Li et. al. 2001), excessive particle motion (Chen et. al. 2004), shell computation (Li and Liu 2000) and fluid mechanics (Iske and Kaeser 2005). In areas such as petroleum and geotechnical engineering only very few applications of meshfree methods can be found yet. The Reproducing Kernel Particle method was utilized in a Lagragian-type formulation to model elastoplastic behaviour in geotechnical material (Wu et. al. 2001). The Smooth Particle Hydrodynamics method (SPH) has its origin in astrophysics modelling star dust clouds (Gingold and Monaghan 1977), but was later on successfully applied in fluid dynamics too. A particular case is the modelling of diffusion processes in porous media (Zhu and Fox 2001). Various geometrical configurations of the porous structure were investigated in order to compute the diffusion coefficients. This research has direct application to oil and gas reservoir simulation. More recently, micropolar elasticity was applied to the local boundary integral equation method (Sladek and Sladek 2003). However, the application of the micropolar continuum was restricted to the two-dimensional case and only linearity in geometry and material was taken into account.

1.2 Thesis motivation, aim and objectives

The variety of methods within the generalized continua as previously outlined shows that it is possible to address the same problems, e.g. size effects exhibited in elasticity, by means of different approaches such as *Cosserat continuum* or strain gradient-based formulations. On the other hand, considering the diversity of problems one is confronted in the mechanics, it is clear that the proposed methods usually tried to reflect closely the physical behaviour associated with certain material. Consequently, they incorporated certain simplifications, restrictions or assumptions, e.g. linearity in geometry or material, so that the area of application was a very narrow one. Now, it is however desirable to develop a generalized formulation based on a non-linear and three-dimensional continuum mechanical theory which allows to deal with a broader range of physical phenomena. That means a theoretical framework which carries in principle a certain universality, but can be easily adapted to the specific properties of a problem.

In this work therefore, the micro- or meso-structure is modelled in a very general manner which is to incorporate the size and the dimension of the micro-continuum into a continuum mechanical approach. The focus however, is primarily set on solid mechanics. The approach is based on a theory developed by Sansour (1998b) which is originated in theoretical considerations of Ericksen and Truesdell (1957) as well as Eringen and his co-workers (Eringen 1975). The basic idea is to construct a generalized continuum consisting of macro- and micro-continuum and subsequently to compose the generalized deformation by a macro- and micro-component. The dimension of the micro-continuum or the number of degrees of freedom additional to those needed for a classical continuum, respectively, may be freely chosen depending on the accuracy of the description of a physical property, but must be finite. The approach considers a geometrically exact description of finite deformation within the macro-continuum, but as a first step linearizes the deformation within the micro-continuum. In general however, this ansatz also allows as to formulation of the micro-deformation non-

linearly. Based on the approach of a generalized deformation new non-linear strain measures can be defined and a generalized variational principle can be formulated. Furthermore, corresponding field equations can be identified. Here it is assumed that the deformation field can only be varied within the macro-continuum so that the balance equations are established for the macro-space. The constitutive law however, is defined at the microscopic level and the geometrical specification of the micro-continuum is the only material input which goes beyond that needed in a classical description.

In this research project three different generalized deformation formulations are derived from the initial unified framework. Two of them are constructed in such a way that no extra degrees of freedom are required which are additional to those in a classical continuum. By a specific definition of the micro-deformation the first approach allows as to describe the orientation of the micro-continuum relative to the macro-continuum, but also micro-shear, whereas the second additionally introduces micro-stretch. The latter can be therefore called generalized micromorph continuum. A special detail of these two approaches is that they involve first order strain gradients. The third approach makes use of a macroscopic rotation field which is considered to be independent of the macroscopic displacement field so that the formulation incorporates three additional rotational degrees of freedom. The rotation field is included in this generalized deformation description by means of the macroscopic rotation tensor. The procedure leads to a generalized micropolar continuum which is closely related to the *Cosserat Continuum*. It may be therefore called generalized Cosserat continuum.

Besides the aim to provide the theoretical framework to address heterogeneous media, this thesis also puts a strong emphasis on modelling generalized continua with meshfree methods. As described previously, meshfree methods clearly have much potential for alleviating some of the difficulties associated with finite element analysis. However, when applying MLS-based meshfree methods to an elliptic partial differential problem the enforcement of the corresponding essential boundary conditions provides difficulties. The reasons for this are twofold. Firstly, the direct and explicit enforcement of essential boundary conditions, which is the common procedure in FEM, is not available for meshfree methods. This is rooted in the fact that the approximation functions do not possess the *Kronecker Delta property*. Secondly, the boundary areas exhibit a limited particle support, as there is no support from outside the problem domain. In order to ensure the minimum necessary support, the influence zones of those particles adjacent to the boundary have to be larger than within the domain. This consequently results in a significantly reduced approximation accuracy at and near the boundary which in fact causes difficulties, if the problem formulation involves boundary integral expressions.

In the context of micropolar continuum-based formulations, a remaining question is the treatment of the independent rotation field using meshfree methods. Considering the rotation tensor to be element of the *Lie* group $SO(3)$ one has to take into account its multiplicative and therefore non-linear structure. That is, the updating of the rotation field is naturally carried out multiplicatively.

Furthermore, the potential in modelling formulations involving higher order derivatives has not been widely recognized and studied yet, except for a few one- and two-dimensional case studies (Askes and Aifantis 2002; Pamin *et al.*, 2003, Tang *et al.*, 2003) which only

considered linear geometry. Nevertheless, the flexibility of MLS-based meshfree methods to design approximation functions which provide any desired continuity strongly aids the aim of this thesis to model with generalized formulations which also involve higher order derivatives.

First of all however, it is necessary to thoroughly investigate the specific properties of the so-called *moving least square method* (MLS) and its use in meshfree methods, i.e. the approximation accuracy of a function and its derivatives, the boundary condition enforcement, the numerical integration and discretization strategies. The findings will help to design continuum mechanical formulations in general. The next step is to study less involved models such as a *Green strain tensor* and a classical *Cosserat continuum*-based formulation, as it is considered to be essential to gather experience which can be applied to the development of more sophisticated approaches. In particular, the multiplicative updating of the independent rotation field of the *Cosserat continuum* needs to be examined, when it is applied to meshfree methods. Widely accepted is the multiplicative updating scheme by Simo and Vu-Quoc (1986) which however, has been proven to be path-dependent (Jelenic and Crisfield 1999). Therefore, this work resorts on a completely different method (Sansour and Wagner 2003b) which is path-independent and also allows to approximate the total rotation field and not only its increment. The main attention however, lies on the modelling with the generalized micromorph and the generalized Cosserat continuum. As a field of application elastic problems exhibiting size-scale effects are chosen. These are elastic bending experiments on epoxy micro-films, torsion of human bone specimens and a large-scale study of excavations in dry rock conglomerate with different geometrical configurations. Differences are highlighted for each model assuming different dimensionality of the micro-space, as well as for the direct comparison of both models to each other, but also to *Green strain tensor* and the conventional *Cosserat continuum*-based model. Moreover, the potential use of the proposed generalized continuum approaches in solid mechanics is illustrated in general.

This thesis is concluded by experiments in modified and mixed formulations involving higher order derivatives. In contrast to the generalized formulations the incorporation of higher order derivatives is here achieved by modifying classical functionals such as the *Hellinger Reissner* and the *Hu-Washizu* functional, or by simply making use of the integral form of the equilibrium equations. It is expected that the order of the used numerical integration scheme, which in this work is the Gauss quadrature, can be lowered corresponding to the derivation order incorporated in the formulation. Moreover, it might allow to utilize a particle integration scheme, as the higher order derivatives might compensate for the vanishing first order derivatives at the particles and thus, stabilize the formulations. The outcome would be a truly meshfree method, as no background grid for the integration would then be needed.

Part of this work is the *C++* implementation of a MLS-based meshfree method and the developed variational formulations. The coding is parallelized making use of the so-called *message parsing interface* (MPI) so that a supercomputer with a distributed memory architecture can be utilized. The efforts devoted to a parallelized implementation is justified considering that meshfree methods generally involve significantly more computation time than e.g. the finite element method due to the larger particle interaction. Furthermore,

the theory and the modelling is focused on the three-dimensional space and no dimensional reduction scheme is applied. Moreover, in case of the generalized continua, the numerical integration over the micro-continuum binds additional computing performance. The *C++* programming language is chosen, because it is an object-oriented language which makes it easy to structure and extend the code. Furthermore, *C++* features a flexible, dynamic memory allocation as well as various so-called standard libraries that facilitate the coding and are already optimized with respect to numerical performance. Additionally, diverse software libraries are available for *C++* such as equation solvers and graph partitioner.

1.3 Layout of the thesis

Sec. 1.1 presents an introduction to the research topic. Subsequently, Sec. 1.2 outlines the motivations, aims and objectives sought by this research project. Finally, a synopsis of the following chapters of this thesis is detailed below.

Chapter 2 gives a brief introduction on the continuum mechanical principles which are needed to account for non-linear problems in solid mechanics. Included are the kinematical relations, strain and stress measures as well as the fundamental balance equations.

In Chapter 3, a detailed description of a MLS-based meshfree method is provided. Its essential construction elements are addressed and the approximation accuracy is thoroughly investigated. Further attention is devoted to implementational issues such as the essential boundary condition enforcement and the numerical integration.

In Chapter 4, a modified variational formulation based on the *Green strain tensor* is presented. Furthermore, a new technique is proposed which allows for the stabilization of this modified variational principle in a flexible and adaptive way. The impact of non-linearity in geometry as well as in material is studied with regard to the boundary condition imposition accuracy and numerical stability. This methodology is demonstrated on shell deformations in non-linear structural mechanics involving two different hyper-elastic material laws.

Chapter 5 is dedicated to the well-known *Cosserat continuum*. The *Cosserat* strain tensors and their variational forms are derived. It is followed by the presentation of a variational principle based on the *Cosserat continuum* which also includes the corresponding equilibrium equations. Further efforts are concentrated on the displacement boundary condition enforcement which is achieved by modifying the original variational formulation. Subsequently, details of a multiplicative rotation updating algorithm are provided and its applicability to the moving least square method is studied. Finally, the proposed modified variational principle is used to model size-scale effects of bone and polymeric specimens making use of the *Saint-Venant-Kirchhoff* constitutive model.

In Chapter 6, the framework of a generalized continuum approach for deformation is introduced. Subsequently, three different models for a generalized deformation are derived from this theory. The first two approaches only involve the conventional displacement degrees. The incorporation of the first order derivatives of the macroscopic deformation field allows in the first model to account for the micro-continuum's orientation as well as micro-shear,

and in the second additionally for micro-stretch. The third approach assumes a micropolar material behaviour which is achieved by the incorporation of the macroscopic rotation tensor and involves three extra rotational degrees of freedom. Various computations demonstrate that those models are able to address fundamental physical phenomena which are related to the underlying microstructure of the material, in particular scale-effects. The computed results are compared with the classical *Green strain tensor*-based formulation presented in Chapter 4 in order to reveal the differences between classical and non-classical formulations. Furthermore, it is shown that the MLS-based meshfree method described in Chapter 3 provides the flexibility in terms of the continuity and consistency requirements needed by the generalized formulations.

In Chapter 7, modified variational principles are introduced which involve higher order derivatives. The first two models are mixed formulations which are based on the *Hellinger-Reissner* functional, another one is originated in the *Hu-Washizu* functional and the last one represents the integral form of the equilibrium equations. The overall aim of this chapter is to study the suitability of MLS-based meshfree methods with respect to the higher order derivatives.

The conclusions drawn from this research project are outlined in Chapter 8.

Finally, Chapter 9 contains suggestions and recommendations for future work on the topic.

Chapter 2

Foundations of continuum mechanics

Problems in continuum mechanics are usually described by boundary value problems which are given in form of field equations and make use of certain kinematical quantities, physical and a material laws. Generally, solution of such problems cannot be achieved analytically so that discretization strategies have to be utilized. In doing so, the problem is transferred into a system of algebraic equations which are solved numerically.

This chapter will provide an introduction to the general foundations dealing with geometrical non-linear problems in continuum mechanics. This includes the kinematics, strain and stress measures and the balance equations. For more details the reader is referred to (Truesdell and Noll 1965; Spencer 1980; Marsden and Hughes 1983; Mase G.T. and Mase G.E. 1999).

2.1 Kinematics and geometry

Let $\mathcal{B} \subset \mathbb{E}(3)$, where $\mathcal{B}$ is a three-dimensional manifold defining a material body. A motion of $\mathcal{B}$ is represented by a one parameter non-linear deformation mapping $\boldsymbol{\varphi}_t : \mathcal{B} \to \mathcal{B}_t$, where $t \in \mathbb{R}$ is the time and $\mathcal{B}_t$ is the current configuration at time t. Accordingly, each material point $\mathbf{X} \in \mathcal{B}$ is related to its placement $\mathbf{x}$ in the spatial configuration $\mathcal{B}_t$ by the mapping

$$\mathbf{x} = \boldsymbol{\varphi}\,(\mathbf{X}, t) \tag{2.1}$$

In what follows and without loss of generality we identify the body $\mathcal{B}$ with its undeformed reference configuration at a fixed time t_0. The deformation map possesses an invertible linear tangent map $\mathbf{F} = \operatorname{Grad} \boldsymbol{\varphi}$ denoted by the deformation gradient, where the Jacobian $J = \det \mathbf{F} > 0$. The operator Grad represents the gradient with respect to the reference configuration

$$\operatorname{Grad} := \frac{\partial}{\partial \mathbf{X}}\,. \tag{2.2}$$

With θ^i, $i = 1, 2, 3$ being the coordinate charts in $\mathcal{B}$ which we assume to be convected, the co-variant base vectors

$$\mathbf{G}_i = \frac{\partial \mathbf{X}}{\partial \theta^i} \qquad \text{with} \qquad \mathbf{G}_i \in \mathcal{T}\mathcal{B} \tag{2.3}$$

and

$$\mathbf{g}_i = \frac{\partial \mathbf{x}}{\partial \theta^i} \qquad \text{with} \qquad \mathbf{g}_i \in \mathcal{T}\mathcal{B}_t \tag{2.4}$$

span the tangent spaces $\mathcal{T}\mathcal{B}$ and $\mathcal{T}\mathcal{B}_t$ associated with $\mathcal{B}$ and $\mathcal{B}_t$ respectively. The corresponding dual contra-variant vectors are denoted by $\mathbf{G}^i$ and $\mathbf{g}^i$, respectively.

The deformation gradient is then alternatively be defined by

$$\mathbf{F}\left(\theta^i, t\right) = \mathbf{g}_i \otimes \mathbf{G}^i \tag{2.5}$$

Here, and in what follows, Latin indices take the values 1, 2 or 3. For the later use we further consider that a volume element in the reference configuration dV can be related to its counterpart in the current configuration dv by

$$dv = \det\left(\mathbf{F}\right)\, dV = J\, dV\,, \tag{2.6}$$

and a surface element in its material configuration dA with its unit normal $\mathbf{n}$ to its counterpart in the spatial configuration da with its unit normal $\boldsymbol{\nu}$ by

$$\boldsymbol{\nu}\, da = \det\left(\mathbf{F}\right)\, \mathbf{F}^{-T}\, \mathbf{n}\, dA\,. \tag{2.7}$$

The material derivative of the *Jacobian* J is expressed by

$$\dot{J} = J\, \mathrm{div}\, \dot{\mathbf{x}}\,, \tag{2.8}$$

where div is the divergence operation in the current configuration.

The displacement field $\mathbf{u}$ is given by

$$\mathbf{u}\left(\theta^i, t\right) = \mathbf{x}\left(\theta^i, t\right) - \mathbf{X}\left(\theta^i\right) \tag{2.9}$$

and with (2.3) we rewrite (2.4) as

$$\mathbf{g}_i\left(\theta^i, t\right) = \mathbf{G}_i + \mathbf{u}_{,i}\,, \tag{2.10}$$

where partial derivatives are denoted by a comma. Thus, the definition of the deformation gradient (2.5) can also be written as

$$\mathbf{F}\left(\theta^i, t\right) = \left(\mathbf{G}_i + \mathbf{u}_{,i}\right) \otimes \mathbf{G}^i\,. \tag{2.11}$$

For later use some additional definitions may be provided. The *Riemannian metrics* are denoted by $\mathbf{G}$ and $\mathbf{g}$ for the reference and the current configuration, respectively. Their co-variant components are given by

$$G_{ij} = \mathbf{G}_i \cdot \mathbf{G}_j \qquad \text{and} \qquad g_{ij} = \mathbf{g}_i \cdot \mathbf{g}_j \tag{2.12}$$

and, correspondingly, the contra-variant components by

$$G^{ij} = \mathbf{G}^i \cdot \mathbf{G}^j \qquad \text{and} \qquad g^{ij} = \mathbf{g}^i \cdot \mathbf{g}^j \,. \tag{2.13}$$

The determinants of the component matrices of $\mathbf{G}$, $\mathbf{g}$ are indicated by G, g, respectively. A Cartesian frame denoted by base vectors $\mathbf{e}_i$ with $i = 1, 2, 3$ is correlated to $\mathbf{G}_i$ by

$$\mathbf{G}_i = c_{ij}\mathbf{e}_j \qquad \text{and} \qquad \mathbf{e}_i = c_{ij}\mathbf{G}^j \tag{2.14}$$

where

$$c_{ij} = \mathbf{G}_i \cdot \mathbf{e}_j \,. \tag{2.15}$$

Furthermore, we have the basic skew-symmetric third order *Levi-Civita tensor* $\boldsymbol{\epsilon}$ (permutation tensor)

$$\boldsymbol{\epsilon} = \epsilon^{ijk}\, \mathbf{G}_i \otimes \mathbf{G}_j \otimes \mathbf{G}_k = \epsilon_{ijk}\, \mathbf{G}^i \otimes \mathbf{G}^j \otimes \mathbf{G}^k \tag{2.16}$$

with its components defined by

$$\epsilon_{ijk} := \sqrt{G}\, e_{ijk} \qquad \text{and} \qquad \epsilon^{ijk} := \frac{1}{\sqrt{G}}\, e^{ijk} \,. \tag{2.17}$$

Its Cartesian components are given by

$$e_{ijk} = e^{ijk} = \begin{cases} 1, & \text{for even permutations of } i, j, k \\ \text{-1}, & \text{for odd permutations of } i, j, k \\ 0, & \text{otherwise} \end{cases} \,. \tag{2.18}$$

The deformation gradient tensor is not invariant with respect to spatial rotations. The rotational part can be extracted by the polar decomposition as follows

$$\mathbf{F} = \mathbf{QU} \quad \text{and} \quad \mathbf{F} = \mathbf{VQ} \tag{2.19}$$

where $\mathbf{U} = \mathbf{U}^T$ and $\mathbf{V} = \mathbf{V}^T$ are the right and the left stretch tensors and $\mathbf{Q}$ is the rotation tensor which is dependent on the deformation, respectively on the map $\boldsymbol{\varphi}(\mathbf{X}, t)$ (Eq. 2.1). That is, $\mathbf{Q}$ is fully determined by means of one of the following symmetry conditions

$$\mathbf{Q}^T\mathbf{F} = \mathbf{F}^T\mathbf{Q} \,, \qquad \mathbf{QF}^T = \mathbf{FQ}^T \,. \tag{2.20}$$

The stretch tensors $\mathbf{U}$ and $\mathbf{V}$ are objective strain measures of a classical continuum and computed by the use the deformation gradient $\mathbf{F}$ and the rotation tensor $\mathbf{Q}$.

The stretch tensors $\mathbf{U}$ and $\mathbf{V}$ can also be associated with the right and left *Cauchy-Green deformation tensor* as follows

$$\mathbf{C} = \mathbf{F}^T\mathbf{F} \quad \text{and} \quad \mathbf{B} = \mathbf{F}\mathbf{F}^T . \tag{2.21}$$

These strain measures can be linked to each other and the following expressions hold

$$\mathbf{V} = \mathbf{Q}\mathbf{U}\mathbf{Q}^T \quad \text{and} \quad \mathbf{C} = \mathbf{U}^2 \quad \text{and} \quad \mathbf{B} = \mathbf{V}^2 \quad \text{and} \quad \mathbf{B} = \mathbf{Q}\mathbf{C}\mathbf{Q}^T . \tag{2.22}$$

The tensors $\mathbf{U}$, $\mathbf{V}$, $\mathbf{C}$ and $\mathbf{B}$ share the property to be equal to $\mathbf{1}$ in the reference configuration. Alternatively, tensors can be defined which vanish in the undeformed configuration. This is the *Green strain tensor* $\mathbf{E}$ and the so-called engineering strain $\mathbf{H}$ defined by

$$\mathbf{E} = \frac{1}{2}\left(\mathbf{C} - \mathbf{1}\right) \quad \text{and} \quad \mathbf{H} = \mathbf{U} - \mathbf{1} . \tag{2.23}$$

2.2 Stress measures

In continuum mechanics the force intensity distribution for a bounded body in the deformed configuration $\mathcal{B}_t$ is expressed with the help of stress measures. The stress in a body corresponds to externally applied body forces $\mathbf{b}$ and surface forces $\mathbf{t}^{(\boldsymbol{\nu})}$, where the second is the so-called *traction vector* acting on a surface with its unit normal vector $\boldsymbol{\nu}$.

Following the *Cauchy stress principle* that the resulting force $\Delta\mathbf{f}$ on surface element Δa which is part of a cutting plane throughout the body $\mathcal{B}_t$ defines in the limit the *traction vector* $\mathbf{t}^{(\boldsymbol{\nu})}$

$$\lim_{\Delta a \to 0} \frac{\Delta \mathbf{f}}{\Delta a} = \frac{d\mathbf{f}}{da} = \mathbf{t}^{(\boldsymbol{\nu})} , \tag{2.24}$$

then the state of stress at each point $\mathbf{x} \in \mathcal{B}_t$ is introduced by the *Cauchy stress lemma*

$$\mathbf{t}^{(\boldsymbol{\nu})}\left(\mathbf{x}, t\right) = \boldsymbol{\sigma}^T\left(\mathbf{x}, t\right)\boldsymbol{\nu}\left(\mathbf{x}, t\right) \tag{2.25}$$

with the *Cauchy stress tensor* $\boldsymbol{\sigma}$ which is a function of the spatial coordinates of $\mathbf{x}$.

If the *Cauchy stress principle* is referred to a differential surface element in the reference configuration dA with its unit normal vector $\mathbf{n}$, the *first Piola-Kirchhoff stress tensor* $\mathbf{P}$ may correspondingly be defined by

$$\mathbf{t}^{(\mathbf{n})}\left(\mathbf{X}, t\right) = \mathbf{P}\left(\mathbf{X}, t\right)\mathbf{n}\left(\mathbf{X}, t\right) \tag{2.26}$$

which is function of the material coordinates $\mathbf{X}$. Additionally, use is often made of the so-called *second Piola-Kirchhoff stress tensor* $\mathbf{S}$ which is linked to $\mathbf{P}$ by

$$\mathbf{P} = \mathbf{F}\mathbf{S}\,. \tag{2.27}$$

Taking into account that the resulting differential force $d\mathbf{f}$ acting on a differential surface element da in the current current configuration and on a differential surface element dA in the reference configuration are equal, the Cauchy stress $\boldsymbol{\sigma}$ can be directly linked to $\mathbf{P}$ by the following relation

$$d\mathbf{f} = \mathbf{P}\mathbf{n}\,dA = \boldsymbol{\sigma}^T\boldsymbol{\nu}\,da = \boldsymbol{\sigma}^T \det(\mathbf{F})\ \mathbf{F}^{-T}\,\mathbf{n}\,dA\,,$$

where we made use of Eq. (2.7). Subsequently, we can extract

$$\mathbf{P} = \det(\mathbf{F})\ \boldsymbol{\sigma}^T\,\mathbf{F}^{-T}\,. \tag{2.28}$$

2.3 Balance Laws of Continuum Mechanics

To complete the framework of continuum mechanics needed within this research project, three fundamental balance laws are introduced. These are the balance laws of mass conservation, linear momentum conservation and angular momentum conservation.

2.3.1 Conservation of mass

The mass m of a material continuum body $\mathcal{B}_t$ at time t is given by

$$m = \int_{\mathcal{B}_t} \rho\,(\mathbf{x},t)\ \ dv\,, \tag{2.29}$$

where ρ is the density in the current configuration. The law of *conservation of mass* asserts that the total mass of a body $\mathcal{B}$, or of any portion of the body, is conserved with motion. Thus, the material derivative of Eq. (2.29) is zero

$$\dot{m} = \frac{d}{dt}\int_{\mathcal{B}_t} \rho\,(\mathbf{x},t)\ \ dv = \int_{\mathcal{B}_t} \left\{\,\dot{\rho}\,(\mathbf{x},t) + \rho\,(\mathbf{x},t)\ J\,\mathrm{div}\,\dot{\mathbf{x}}\,\right\}\ dv = 0\,, \tag{2.30}$$

where the relations (Eq. 2.6) and (Eq. 2.8) were used. Since $\mathcal{B}_t$ is any arbitrary part of the continuum the integrand in Eq. (2.30) must vanish, resulting in the so-called *continuity equation* in the Eulerian form

$$\dot{\rho}\,(\mathbf{x},t) + \rho\,(\mathbf{x},t)\ J\,\mathrm{div}\,\dot{\mathbf{x}} = 0\,. \tag{2.31}$$

The conservation of mass also states that the mass in the current and the reference configuration are equal

$$m = \int_{\mathcal{B}_t} \rho\,(\mathbf{x}, t)\ dv = \int_{\mathcal{B}} \rho_0\,(\mathbf{X})\ dV\,, \tag{2.32}$$

where ρ_0 denotes the density in the reference configuration. With Eq. (2.6) and considering $\mathbf{x} = \mathbf{x}(\mathbf{X}, t)$, Eq. (2.29) can also be expressed in its Lagrangian form by

$$m = \int_{\mathcal{B}} \rho\,(\mathbf{X}, t)\ J\ dV\,, \tag{2.33}$$

and substituting this equation for the left-hand side of Eq. (2.32) we arrive at

$$\int_{\mathcal{B}} \Big\{\ \rho\,(\mathbf{X}, t)\ J - \rho_0\,(\mathbf{X})\ \Big\}\ dV = 0\,. \tag{2.34}$$

This must be again valid for any arbitrary part of the continuum and we have the Lagrangian or material form of the continuity equation

$$\rho\,(\mathbf{X}, t)\ J = \rho_0\,(\mathbf{X})\ . \tag{2.35}$$

With $\dot{\rho_0} = 0$ we further have

$$\frac{d}{dt}\Big(\rho\,(\mathbf{X}, t)\ J\Big) = 0\,. \tag{2.36}$$

This equation in particular, is very useful to evaluate the material derivative of an integral over some product $\rho\, A$

$$\frac{d}{dt}\int_{\mathcal{B}_t} \rho\,(\mathbf{x}, t)\ A(\mathbf{x}, t)\ dv = \int_{\mathcal{B}_t} \rho\,(\mathbf{x}, t)\ \dot{A}(\mathbf{x}, t)\ dv\,, \tag{2.37}$$

where $A(\mathbf{x}, t)$ is a field of some property per unit mass.

2.3.2 Linear momentum principle

Consider a material continuum body $\mathcal{B}$ subjected to body force $\mathbf{b}$ and a bounding surface $\partial\mathcal{B}$ subjected to surface traction $\mathbf{t}^{(\boldsymbol{\nu})}$. Then the principle of linear momentum asserts that the time rate of change of the linear momentum equals the resultant force acting on the body

$$\frac{d}{dt}\int_{\mathcal{B}_t} \rho\,(\mathbf{x}, t)\ \dot{\mathbf{x}}\ dv = \int_{\partial\mathcal{B}_t} \mathbf{t}^{(\boldsymbol{\nu})}\,(\mathbf{x}, t)\ da + \int_{\mathcal{B}_t} \mathbf{b}\,(\mathbf{x}, t)\ dv\,. \tag{2.38}$$

Making use of the *Cauchy stress lemma* (Eq. 2.25) and *Gauss's divergence theorem* we can rewrite Eq. (2.38) so that we arrive at the *global equation of motion* in its spatial form

$$\int_{\mathcal{B}_t} \left\{ \rho\left(\mathbf{x},t\right)\, \ddot{\mathbf{x}} - \operatorname{div} \boldsymbol{\sigma}^T - \mathbf{b}\left(\mathbf{x},t\right) \right\} dv = \mathbf{0}\,, \tag{2.39}$$

where Eq. (2.37) has been used to evaluate the material time derivative. The corresponding *local equation of motion* follows considering that $\mathcal{B}_t$ is arbitrary and therefore the integrand in Eq. (2.38) must vanish

$$\operatorname{div} \boldsymbol{\sigma}^T + \mathbf{b}\left(\mathbf{x},t\right) = \rho\left(\mathbf{x},t\right)\, \ddot{\mathbf{x}}\,. \tag{2.40}$$

If the velocity field $\dot{\mathbf{x}}\left(\mathbf{x},t\right)$ is constant or zero, the equation of motion reduces to the so-called *equilibrium equation*

$$\operatorname{div} \boldsymbol{\sigma}^T + \mathbf{b}\left(\mathbf{x},t\right) = \mathbf{0}\,. \tag{2.41}$$

We further have the *global equation of motion* in its material form by referring all quantities in Eq. (2.38) to the reference configuration

$$\frac{d}{dt} \int_{\mathcal{B}} \rho_0\, \dot{\mathbf{x}}\left(\mathbf{X},t\right)\, dV = \int_{\partial\mathcal{B}} \mathbf{t}^{(\mathbf{n})}\left(\mathbf{X},t\right)\, dA + \int_{\mathcal{B}} \mathbf{b}\left(\mathbf{X},t\right)\, dV\,. \tag{2.42}$$

Subsequently, we replace the traction vector by Eq. (2.26), apply *Gauss's divergence theorem*, take material derivative of the left-hand side and arrive at

$$\int_{\mathcal{B}} \left\{ \rho_0\, \ddot{\mathbf{x}}\left(\mathbf{X},t\right) - \operatorname{Div} \mathbf{P} - \mathbf{b}\left(\mathbf{X},t\right) \right\} dV = \mathbf{0}\,, \tag{2.43}$$

where Div stands for the divergence operator with respect to the reference configuration. The integral over $\mathcal{B}$ is arbitrary and the integrand in Eq. (2.43) must vanish

$$\operatorname{Div} \mathbf{P} + \mathbf{b}\left(\mathbf{X},t\right) = \rho_0\, \ddot{\mathbf{x}}\left(\mathbf{X},t\right)\,, \tag{2.44}$$

which is the *Lagrangian equation of motion*. If the acceleration field is zero, we have the *Lagrangian equilibrium equation*

$$\operatorname{Div} \mathbf{P}\left(\mathbf{X},t\right) + \mathbf{b}\left(\mathbf{X},t\right) = \mathbf{0}\,. \tag{2.45}$$

2.3.3 Angular momentum principle

The angular momentum is defined as the *moment of the linear momentum* with respect to some reference point. This point of reference is usually chosen to be the origin of some coordinate system. The angular momentum principle asserts that the time rate of change of the moment of linear momentum is equal to the resultant moment of the surface and body forces acting on the body $\mathcal{B}$:

$$\frac{d}{dt}\int\limits_{\mathcal{B}_t} \mathbf{x}\times\rho\left(\mathbf{x},t\right)\,\dot{\mathbf{x}}\;dv = \int\limits_{\partial\mathcal{B}_t} \mathbf{x}\times\mathbf{t}^{(\boldsymbol{\nu})}\left(\mathbf{x},t\right)\;da + \int\limits_{\mathcal{B}_t} \mathbf{x}\times\mathbf{b}\left(\mathbf{x},t\right)\;\;dv\,. \tag{2.46}$$

Taking the material derivative of the left-hand side with the help of Eq. (2.37), introducing the *Cauchy stress tensor* with Eq. (2.25) and subsequently applying *Gauss's divergence theorem*, we have:

$$\int\limits_{\mathcal{B}_t}\left\{\mathbf{x}\times\rho\left(\mathbf{x},t\right)\,\ddot{\mathbf{x}} - \operatorname{div}\left(\mathbf{x}\times\boldsymbol{\sigma}^T\right) - \mathbf{x}\times\mathbf{b}\left(\mathbf{x},t\right)\right\}\,dv = \mathbf{0}\,, \tag{2.47}$$

where the divergence term with respect to the current configuration is evaluated as follows

$$\operatorname{div}\left(\mathbf{x}\times\boldsymbol{\sigma}^T\right) = \operatorname{grad}\mathbf{x}\times\boldsymbol{\sigma}^T + \mathbf{x}\times\operatorname{div}\boldsymbol{\sigma}^T\,. \tag{2.48}$$

For the definition of the product $\mathbf{x}\times\boldsymbol{\sigma}^T$ the reader is referred to App. D. The relation holds $\operatorname{grad}\mathbf{x} = \mathbf{1}$ and the global principle of angular momentum in its spatial form is expressed by

$$\int\limits_{\mathcal{B}_t}\left\{\mathbf{x}\times\rho\left(\mathbf{x},t\right)\,\ddot{\mathbf{x}} + \boldsymbol{\epsilon}:\boldsymbol{\sigma}^T - \mathbf{x}\times\operatorname{div}\boldsymbol{\sigma}^T - \mathbf{x}\times\mathbf{b}\left(\mathbf{x},t\right)\right\}\,dv = \mathbf{0}\,. \tag{2.49}$$

For the definition of the tensor product $\boldsymbol{\epsilon}:\boldsymbol{\sigma}^T$ the reader is again referred to App. D. The corresponding field equation is expressed by

$$\mathbf{x}\times\rho\left(\mathbf{x},t\right)\,\ddot{\mathbf{x}} - \mathbf{x}\times\operatorname{div}\boldsymbol{\sigma}^T - \mathbf{x}\times\mathbf{b}\left(\mathbf{x},t\right) + \boldsymbol{\epsilon}:\boldsymbol{\sigma}^T = \mathbf{0}\,, \tag{2.50}$$

because $\mathcal{B}_t$ is arbitrary and the integrand in Eq. (2.49) must vanish. With Eq. (2.40) we further have

$$\boldsymbol{\epsilon}:\boldsymbol{\sigma}^T = \mathbf{0}\,, \tag{2.51}$$

which shows the symmetry of the Cauchy stress tensor. Note it is assumed in this chapter that no surface couple acts on the body.

The angular momentum principle in the Lagrangian form is achieved by referring all quantities in Eq. (2.46) to the reference configuration

$$\frac{d}{dt}\int_{\mathcal{B}} \mathbf{x}(\mathbf{X},t)\times\rho_0\,\dot{\mathbf{x}}(\mathbf{X},t)\;dV \;=\; \int_{\partial\mathcal{B}} \mathbf{x}(\mathbf{X},t)\times\mathbf{t}^{(\mathbf{n})}(\mathbf{X},t)\;dA \;+\; \int_{\mathcal{B}} \mathbf{x}(\mathbf{X},t)\times\mathbf{b}(\mathbf{X},t)\;dV\,. \tag{2.52}$$

After taking material derivative of the left-hand side, the traction vector is replaced by Eq. (2.26) and *Gauss's divergence theorem* is applied so that we arrive at

$$\int_{\mathcal{B}} \Big\{ \mathbf{x}(\mathbf{X},t)\times\rho_0\,\ddot{\mathbf{x}}(\mathbf{X},t) - \\ -\operatorname{Div}\Big(\mathbf{x}(\mathbf{X},t)\times\mathbf{P}\Big) - \mathbf{x}(\mathbf{X},t)\times\mathbf{b}(\mathbf{X},t)\Big\}\,dV = \mathbf{0}\,. \tag{2.53}$$

The evaluation of the divergence term similar to Eq. (2.48) leads to

$$\int_{\mathcal{B}} \Big\{ \mathbf{x}(\mathbf{X},t)\times\big(\rho_0\,\ddot{\mathbf{x}}(\mathbf{X},t) - \operatorname{Div}\mathbf{P} - \mathbf{b}(\mathbf{X},t)\big) - \\ -\operatorname{Grad}\mathbf{x}(\mathbf{X},t)\times\mathbf{P}\Big\}\,dV = \mathbf{0}\,, \tag{2.54}$$

and with Eq. (2.44) we have the following expression

$$\int_{\mathcal{B}} \mathbf{F}\times\mathbf{P}\;dV = \mathbf{0}\,. \tag{2.55}$$

The integrand must vanish

$$\mathbf{F}\times\mathbf{P} = \boldsymbol{\epsilon} : \big(\mathbf{F}\mathbf{P}^T\big) = \mathbf{0}\,, \tag{2.56}$$

which results in the following symmetry condition

$$\mathbf{F}\mathbf{P}^T = \mathbf{P}\mathbf{F}^T\,. \tag{2.57}$$

The substition of Eq. (2.27) for $\mathbf{P}$ finally results in the symmetry of the *second Piola-Kirchhoff tensor*

$$\mathbf{S}^T = \mathbf{S}\,. \tag{2.58}$$

In the following and throughout this thesis all expressions will be written in the material description. The focus will be exclusively on a purely mechanical theory within three-dimensional elasticity, thermal and other effects are not considered.

Chapter 3

Meshfree methods

It is an essential aim of this research project to model problems which also involve higher order derivatives of the solution function. The flexibility of *moving least square* (MLS)-based meshfree methods to design approximation functions which provide any desired continuity, greatly aids this purpose. Therefore, a MLS-based meshfree method is utilized for the modelling with the formulations developed later on in this thesis.

The outline of the this chapter is as follows: A detailed description of the basic principles a MLS-based meshfree method and its core components is given in Sec. 3.1. As it is considered to be essential to gain more insight in the MLS-approximation properties, Sec. 3.2 is devoted to MLS and its construction elements for their impact on the approximation accuracy. In Sec. 3.3 implementational issues are addressed which includes the essential boundary condition enforcement and the numerical integration. Notes regarding the parallelization of the meshfree code are provided in App. B.

3.1 Meshfree approximation based on MLS

In this work a meshfree method is implemented which is based on the *moving least square method* and improvements suggested in element-free Galerkin and reproducing kernel particle method such as the normalized weight function, the shifted polynomial basis and the numerical integration over the least square fit are incorporated. In the following MLS is briefly outlined. Subsequently, important characteristics such as the weight function and the polynomial basis are elaborated in more detail.

3.1.1 Moving Least Square Method

MLS has been originally introduced as data-fitting algorithm, where an approximation of a function is constructed based on a given set of particles. Let us consider a function $u(\mathbf{x})$ defined over the field $\Omega \in \mathbb{R}^3$. A possible approximation for $u(\mathbf{x})$ is defined by a complete

polynomial $\mathbf{P}(\mathbf{x})$ and its non-constant coefficients $\mathbf{a}(\mathbf{x})$:

$$u^h(\mathbf{x}) = \mathbf{P}(\mathbf{x}) \cdot \mathbf{a}(\mathbf{x}) \ . \tag{3.1}$$

To each particle P_I with its coordinates $\mathbf{x}_I$, a so-called weight function Φ_I with compact support is attached. That is, the size of the support is defined by the so-called *influence radius* ϱ. The sum of all particles, that support the point $\mathbf{x}$, constitute the set Λ. With the help of this set a weighted least square fit in the vicinity of a point $\mathbf{x}$ can be constructed according to

$$J(\mathbf{a}(\mathbf{x})) := \sum_{I \in \Lambda} \left[\mathbf{P}(\mathbf{x}_I) \cdot \mathbf{a}(\mathbf{x}) - u(\mathbf{x}_I)\right]^2 \Phi\left(\frac{\mathbf{x} - \mathbf{x}_I}{\varrho}\right) \ . \tag{3.2}$$

Thereby, the locality of the least square fit is controlled by the weight function Φ and the influence radius ϱ, respectively. That is, only those particles in the closest neighbourhood of x are taken into the computation of the least square fit (Eq. 3.2) and the minimization of the difference between approximated function values $u^h(\mathbf{x}_I)$ and exact ones $u(\mathbf{x}_I)$ is emphasized the closer a particle is placed to $\mathbf{x}$.

The unknown coefficients $\mathbf{a}(\mathbf{x})$ can be determined by minimizing the functional J (Eq. 3.2) with respect to $\mathbf{a}(\mathbf{x})$. Then the substitution of the coefficients $\mathbf{a}(\mathbf{x})$ into (Eq. 3.1) provides the approximation of $u(\mathbf{x})$ as follows

$$u^h(\mathbf{x}) = \mathbf{P}(\mathbf{x}) \cdot \mathbf{M}^{-1}(\mathbf{x}) \sum_{I \in \Lambda} \mathbf{P}(\mathbf{x}_I) \ \Phi\left(\frac{\mathbf{x} - \mathbf{x}_I}{\varrho}\right) \ u_I \, , \tag{3.3}$$

where $\mathbf{M}(\mathbf{x})$ is the so-called *moment matrix* of the weight function Φ:

$$\mathbf{M}(\mathbf{x}) = \sum_{I = \Lambda} \mathbf{P}(\mathbf{x}_I) \, \mathbf{P}(\mathbf{x}_I) \, \Phi\left(\frac{\mathbf{x} - \mathbf{x}_I}{\varrho}\right) \ , \tag{3.4}$$

and u_I are the so-called particle parameters. The MLS-approximation function for a particle P_I can be expressed by

$$N_I(\mathbf{x}) = \mathbf{P}(\mathbf{x}) \cdot \mathbf{M}^{-1}(\mathbf{x}) \, \mathbf{P}(\mathbf{x}_I) \ \Phi\left(\frac{\mathbf{x} - \mathbf{x}_I}{\varrho}\right) \ , \tag{3.5}$$

and (Eq. 3.3) takes

$$u^h(\mathbf{x}) = \sum_{I \in \Lambda} N_I(\mathbf{x}) \ u_I \, . \tag{3.6}$$

The terminology *moving least square* is related to the consideration that the point $\mathbf{x}$ may be any point $P \in \Omega$. This means that by "moving" $\mathbf{x}$ throughout the domain Ω the approximation $u^h(\mathbf{x})$ (Eq. 3.3) is transferred from a local to a global approximation.

Since the least square fit (Eq. 3.2) is weighted by function Φ which has compact support, the local character of the approximation $u^h(\mathbf{x})$ is ensured. Consequently, the accuracy of the approximation $u^h(\mathbf{x})$ is optimized the smaller the value of ϱ is chosen. The minimum value of ϱ is however restricted by the invertibility requirement of the moment matrix (Eq. 3.4). That is, the minimum number supporting particles for a point $\mathbf{x}$ must be equal or larger than the number of elements in the basis polynomial $\mathbf{P}$. Considering that due to the locality of the weight function the influence of a particle and its shape function ordinate over $\mathbf{x}$, respectively, is usually rapidly deferring with increasing distance to point $\mathbf{x}$, the number of supporting particles must be higher than the minimum needed. Especially, for an irregular particle distribution we find that the particle support is up to ten times as high than minimal required. Note that for each point $\mathbf{x}$ the weighted least square fit (Eq. 3.2) needs to be separately evaluated which results in a unique and local approximation for each point $\mathbf{x}$.

The basic technique applied in this algorithm is the so-called *inverse distance weighted principle*. The simplest form of an approximation constructed by this principle is by the so-called *Shepard-method*

$$u^h(\mathbf{x}) = \sum_{I \in \Lambda} \frac{\Phi\left(\frac{\mathbf{x}-\mathbf{x}_I}{\varrho}\right)}{\sum\limits_{J \in \Lambda} \Phi\left(\frac{\mathbf{x}-\mathbf{x}_J}{\varrho}\right)} u_I \,, \tag{3.7}$$

which is equivalent to a MLS interpolation using a zero order basis polynomial $\mathbf{P}(\mathbf{x}) = 1$.

The smoothness of the MLS approximation is determined by the invertibility requirement of Eq. (3.4) as well by Eq. (3.3). This is as both expressions depend on the continuity of the basis polynomial $\mathbf{P} \in C^m(\Omega)$ as well as the weight function $\Phi \in C^l(\Omega)$ and it holds

$$u^h(\mathbf{x}) \in C^k \tag{3.8}$$

with $k = \min(l, m)$ (Lancaster and Salkauskas 1981).

The consistency conditions on the MLS-approximants, that is, the requirement to reproduce a polynomial of a certain order

$$\sum_{I \in \Lambda} N_I(\mathbf{x})\ \mathbf{P}(\mathbf{x}_I) = \mathbf{P}(\mathbf{x})\ , \tag{3.9}$$

have been proven to be fulfilled (Belytschko *et al.* 1996), as these conditions are incorporated in the MLS-algorithm. In particular, it has been shown that a MLS-approximation exactly represents its basis polynomial. The so-called *partition of unity* condition

$$\sum_{I \in \Lambda} N_I(\mathbf{x}) = 1\,, \tag{3.10}$$

which is imperative to reproduce rigid body motions correctly (Liu *et al.* 1995), is always satisfied as it means to reproduce a constant polynomial $\mathbf{P} = 1$ which is achieved, if a zero order basis polynomial is used in Eq. (3.5).

The computation of the MLS-approximants can be accelerated (Dolbow and Belytschko 1998), if the expression $\mathbf{P}(\mathbf{x}) \cdot \mathbf{M}^{-1}(\mathbf{x})$ in Eq. (3.5) is replaced by a vector $\mathbf{b}(\mathbf{x})$ and we can write

$$N_I(\mathbf{x}) = \mathbf{b}(\mathbf{x})\,\mathbf{P}(\mathbf{x}_I)\;\Phi\left(\frac{\mathbf{x}-\mathbf{x}_I}{\varrho}\right), \tag{3.11}$$

where $\mathbf{b}(\mathbf{x})$ is computed by solving the following linear equation system

$$\mathbf{M}(\mathbf{x})\,\mathbf{b}(\mathbf{x}) = \mathbf{P}(\mathbf{x}). \tag{3.12}$$

Note that this linear equation system is nothing else than consistency conditions (Eq. 3.9). Similarly, the first order partial derivatives of vector $\mathbf{b}(\mathbf{x})$ which are needed for the MLS-shapefunction derivatives can be obtained by solving the following expressions with respect to $\mathbf{b}_{,x}(\mathbf{x})$, $\mathbf{b}_{,y}(\mathbf{x})$ and $\mathbf{b}_{,z}(\mathbf{x})$

$$\begin{aligned}
\frac{\partial \mathbf{M}(\mathbf{x})}{\partial x}\mathbf{b}(\mathbf{x}) + \mathbf{M}(\mathbf{x})\frac{\partial \mathbf{b}(\mathbf{x})}{\partial x} &= \frac{\partial \mathbf{P}(\mathbf{x})}{\partial x},\\
\frac{\partial \mathbf{M}(\mathbf{x})}{\partial y}\mathbf{b}(\mathbf{x}) + \mathbf{M}(\mathbf{x})\frac{\partial \mathbf{b}(\mathbf{x})}{\partial y} &= \frac{\partial \mathbf{P}(\mathbf{x})}{\partial y},\\
\frac{\partial \mathbf{M}(\mathbf{x})}{\partial z}\mathbf{b}(\mathbf{x}) + \mathbf{M}(\mathbf{x})\frac{\partial \mathbf{b}(\mathbf{x})}{\partial z} &= \frac{\partial \mathbf{P}(\mathbf{x})}{\partial z},
\end{aligned} \tag{3.13}$$

where $\mathbf{b}(\mathbf{x})$ computed by Eq. (3.12) is substituted. The second order partial derivatives $\mathbf{b}_{,xy}(\mathbf{x})$, $\mathbf{b}_{,yz}(\mathbf{x})$, $\mathbf{b}_{,zx}(\mathbf{x})$, $\mathbf{b}_{,xx}(\mathbf{x})$, $\mathbf{b}_{,yy}(\mathbf{x})$ and $\mathbf{b}_{,zz}(\mathbf{x})$ are determined by solving

$$\begin{aligned}
\frac{\partial^2 \mathbf{M}(\mathbf{x})}{\partial x\partial y}\mathbf{b}(\mathbf{x}) + \frac{\partial \mathbf{M}(\mathbf{x})}{\partial x}\frac{\partial \mathbf{b}(\mathbf{x})}{\partial y} + \frac{\partial \mathbf{M}(\mathbf{x})}{\partial y}\frac{\partial \mathbf{b}(\mathbf{x})}{\partial x} + \mathbf{M}(\mathbf{x})\frac{\partial^2 \mathbf{b}(\mathbf{x})}{\partial x\partial y} &= \frac{\partial^2 \mathbf{P}(\mathbf{x})}{\partial x\partial y},\\
\frac{\partial^2 \mathbf{M}(\mathbf{x})}{\partial y\partial z}\mathbf{b}(\mathbf{x}) + \frac{\partial \mathbf{M}(\mathbf{x})}{\partial y}\frac{\partial \mathbf{b}(\mathbf{x})}{\partial z} + \frac{\partial \mathbf{M}(\mathbf{x})}{\partial z}\frac{\partial \mathbf{b}(\mathbf{x})}{\partial y} + \mathbf{M}(\mathbf{x})\frac{\partial^2 \mathbf{b}(\mathbf{x})}{\partial y\partial z} &= \frac{\partial^2 \mathbf{P}(\mathbf{x})}{\partial y\partial z},\\
\frac{\partial^2 \mathbf{M}(\mathbf{x})}{\partial z\partial x}\mathbf{b}(\mathbf{x}) + \frac{\partial \mathbf{M}(\mathbf{x})}{\partial z}\frac{\partial \mathbf{b}(\mathbf{x})}{\partial x} + \frac{\partial \mathbf{M}(\mathbf{x})}{\partial x}\frac{\partial \mathbf{b}(\mathbf{x})}{\partial z} + \mathbf{M}(\mathbf{x})\frac{\partial^2 \mathbf{b}(\mathbf{x})}{\partial z\partial x} &= \frac{\partial^2 \mathbf{P}(\mathbf{x})}{\partial z\partial x},
\end{aligned}$$

$$\begin{aligned}
\frac{\partial^2 \mathbf{M}(\mathbf{x})}{\partial x\partial x}\mathbf{b}(\mathbf{x}) + 2\frac{\partial \mathbf{M}(\mathbf{x})}{\partial x}\frac{\partial \mathbf{b}(\mathbf{x})}{\partial x} + \mathbf{M}(\mathbf{x})\frac{\partial^2 \mathbf{b}(\mathbf{x})}{\partial x\partial x} &= \frac{\partial^2 \mathbf{P}(\mathbf{x})}{\partial x\partial x},\\
\frac{\partial^2 \mathbf{M}(\mathbf{x})}{\partial y\partial y}\mathbf{b}(\mathbf{x}) + 2\frac{\partial \mathbf{M}(\mathbf{x})}{\partial y}\frac{\partial \mathbf{b}(\mathbf{x})}{\partial y} + \mathbf{M}(\mathbf{x})\frac{\partial^2 \mathbf{b}(\mathbf{x})}{\partial y\partial y} &= \frac{\partial^2 \mathbf{P}(\mathbf{x})}{\partial y\partial y},\\
\frac{\partial^2 \mathbf{M}(\mathbf{x})}{\partial z\partial z}\mathbf{b}(\mathbf{x}) + 2\frac{\partial \mathbf{M}(\mathbf{x})}{\partial z}\frac{\partial \mathbf{b}(\mathbf{x})}{\partial z} + \mathbf{M}(\mathbf{x})\frac{\partial^2 \mathbf{b}(\mathbf{x})}{\partial z\partial z} &= \frac{\partial^2 \mathbf{P}(\mathbf{x})}{\partial z\partial z},
\end{aligned} \tag{3.14}$$

where $\mathbf{b}(\mathbf{x})$, $\mathbf{b}_{,x}(\mathbf{x})$, $\mathbf{b}_{,y}(\mathbf{x})$ and $\mathbf{b}_{,z}(\mathbf{x})$ computed by by Eq. (3.12) and by Eq. (3.13), respectively, are substituted. Note, before solving Eq. (3.12) - Eq. (3.14) with respect to vector $\mathbf{b}(\mathbf{x})$ and its derivatives, respectively, the *moment matrix* (Eq. (3.4) should be pre-conditioned by LU-factorization.

In case of an irregular particle distribution the *moment matrix* can be ill conditioned. As this matrix must be inverted, it was suggested by Liu *et al.* (1997) to make use of a so-called *shifted basis* which can be additionally normalized by the influence radius ϱ. The moment matrix is then given by the following expression

$$\mathbf{M}(\mathbf{x}) = \sum_{I=\Lambda} \mathbf{P}\left(\frac{\mathbf{x}-\mathbf{x}_I}{\varrho}\right) \mathbf{P}\left(\frac{\mathbf{x}-\mathbf{x}_I}{\varrho}\right) \Phi\left(\frac{\mathbf{x}-\mathbf{x}_I}{\varrho}\right) . \tag{3.15}$$

Accordingly, Eq. (3.12), Eq. (3.13) and Eq. 3.13) take

$$\mathbf{M}(\mathbf{x})\,\mathbf{b}(\mathbf{x}) = \mathbf{P}(\mathbf{0}) , \tag{3.16}$$

$$\begin{aligned}
&\frac{\partial \mathbf{M}(\mathbf{x})}{\partial x}\mathbf{b}(\mathbf{x}) + \mathbf{M}(\mathbf{x})\frac{\partial \mathbf{b}(\mathbf{x})}{\partial x} = \mathbf{0} ,\\
&\frac{\partial \mathbf{M}(\mathbf{x})}{\partial y}\mathbf{b}(\mathbf{x}) + \mathbf{M}(\mathbf{x})\frac{\partial \mathbf{b}(\mathbf{x})}{\partial y} = \mathbf{0} ,\\
&\frac{\partial \mathbf{M}(\mathbf{x})}{\partial z}\mathbf{b}(\mathbf{x}) + \mathbf{M}(\mathbf{x})\frac{\partial \mathbf{b}(\mathbf{x})}{\partial z} = \mathbf{0} ,
\end{aligned} \tag{3.17}$$

and

$$\begin{aligned}
&\frac{\partial^2 \mathbf{M}(\mathbf{x})}{\partial x \partial y}\mathbf{b}(\mathbf{x}) + \frac{\partial \mathbf{M}(\mathbf{x})}{\partial x}\frac{\partial \mathbf{b}(\mathbf{x})}{\partial y} + \frac{\partial \mathbf{M}(\mathbf{x})}{\partial y}\frac{\partial \mathbf{b}(\mathbf{x})}{\partial x} + \mathbf{M}(\mathbf{x})\frac{\partial^2 \mathbf{b}(\mathbf{x})}{\partial x \partial y} = \mathbf{0} ,\\
&\frac{\partial^2 \mathbf{M}(\mathbf{x})}{\partial y \partial z}\mathbf{b}(\mathbf{x}) + \frac{\partial \mathbf{M}(\mathbf{x})}{\partial y}\frac{\partial \mathbf{b}(\mathbf{x})}{\partial z} + \frac{\partial \mathbf{M}(\mathbf{x})}{\partial z}\frac{\partial \mathbf{b}(\mathbf{x})}{\partial y} + \mathbf{M}(\mathbf{x})\frac{\partial^2 \mathbf{b}(\mathbf{x})}{\partial y \partial z} = \mathbf{0} ,\\
&\frac{\partial^2 \mathbf{M}(\mathbf{x})}{\partial z \partial x}\mathbf{b}(\mathbf{x}) + \frac{\partial \mathbf{M}(\mathbf{x})}{\partial z}\frac{\partial \mathbf{b}(\mathbf{x})}{\partial x} + \frac{\partial \mathbf{M}(\mathbf{x})}{\partial x}\frac{\partial \mathbf{b}(\mathbf{x})}{\partial z} + \mathbf{M}(\mathbf{x})\frac{\partial^2 \mathbf{b}(\mathbf{x})}{\partial z \partial x} = \mathbf{0} ,\\
&\frac{\partial^2 \mathbf{M}(\mathbf{x})}{\partial x \partial x}\mathbf{b}(\mathbf{x}) + 2\,\frac{\partial \mathbf{M}(\mathbf{x})}{\partial x}\frac{\partial \mathbf{b}(\mathbf{x})}{\partial x} + \mathbf{M}(\mathbf{x})\frac{\partial^2 \mathbf{b}(\mathbf{x})}{\partial x \partial x} = \mathbf{0} ,\\
&\frac{\partial^2 \mathbf{M}(\mathbf{x})}{\partial y \partial y}\mathbf{b}(\mathbf{x}) + 2\,\frac{\partial \mathbf{M}(\mathbf{x})}{\partial y}\frac{\partial \mathbf{b}(\mathbf{x})}{\partial y} + \mathbf{M}(\mathbf{x})\frac{\partial^2 \mathbf{b}(\mathbf{x})}{\partial y \partial y} = \mathbf{0} ,\\
&\frac{\partial^2 \mathbf{M}(\mathbf{x})}{\partial z \partial z}\mathbf{b}(\mathbf{x}) + 2\,\frac{\partial \mathbf{M}(\mathbf{x})}{\partial z}\frac{\partial \mathbf{b}(\mathbf{x})}{\partial z} + \mathbf{M}(\mathbf{x})\frac{\partial^2 \mathbf{b}(\mathbf{x})}{\partial z \partial z} = \mathbf{0} ,
\end{aligned} \tag{3.18}$$

respectively, where $\mathbf{P}(\mathbf{0}) = [\,1,\,0,\,\ldots,\,0\,]$.

Liu and his co-workers (see e.g. Li and Liu 1998) suggested in their RKPM that the accuracy of the MLS algorithm was improved, if the summation over the residuals of exact and approximated function values in Eq. (3.2) was replaced by a numerical integration. They proposed to use a numerical integration method, the so-called *Nyström method* (Delves and Mohamed 1985), which is a particle integration scheme. Consequently, the summation in Eq. (3.3) and Eq. (3.4) was also replaced by a continuous integral expression. Each particle P_I was associated with an integration weight ΔV_I which corresponded to the particle's share on the system volume

$$\sum_{I \in \Lambda} \Delta V_I = V \,. \tag{3.19}$$

Furthermore, it was proposed, as continuum mechanical formulations are usually numerically integrated by the *Gauss* quadrature, that an underlying FEM-background mesh could not only be utilized to obtain the coordinates and weights of Gaussian integration weights, but also the particle weights ΔV_I as follows

$$\Delta V_I = \sum_{\Lambda_e} J\left(\xi_I, \eta_I, \zeta_I\right) \,, \tag{3.20}$$

where J is the *Jacobian* and the Λ_e is a set of background mesh elements which incorporate particle P_I. Now, the equation for the *moment matrix* (Eq. 3.4) takes the following form

$$\mathbf{M}\left(\mathbf{x}\right) = \sum_{I=\Lambda} \mathbf{P}\left(\mathbf{x}_I\right) \mathbf{P}\left(\mathbf{x}_I\right) \Phi\left(\frac{\mathbf{x}-\mathbf{x}_I}{\varrho}\right) \Delta V_I \,, \tag{3.21}$$

and the MLS-approximation formula (Eq. 3.3) is expressed by

$$\mathbf{u}^h\left(\mathbf{x}\right) = \mathbf{b}\left(\mathbf{x}\right) \sum_{I \in \Lambda} \mathbf{P}\left(\mathbf{x}_I\right) \, \Phi\left(\frac{\mathbf{x}-\mathbf{x}_I}{\varrho}\right) \, \mathbf{u}_I \, \Delta V_I \,. \tag{3.22}$$

Now it is important to realize that MLS was originally considered as curve fitting algorithm, where the sample points $u(\mathbf{x}_I)$ were known. When MLS is used in a meshfree methods however, these sample point values are unknown. That is, the MLS-approximation (Eq. 3.3) with unknown particle parameters u_I is implemented in a formulation which describes the physical state of body. Subsequently, the integration over the problem domain results in a discrete equation system. The solution of this discrete equation system are particle parameters u_I which are determined in such a way that the difference to the exact function values $u(\mathbf{x}_I)$ is as minimal as possible and the approximation $u^h\left(\mathbf{x}\right)$ is a solution of the problem formulation. In fact, there is usually quite a significant difference between u_I and $u(\mathbf{x}_I)$ due to the limited approximation capability of the utilized basis polynomial. Therefore, it must be stressed that we usually have

$$u_I \neq u(\mathbf{x}_I) \,, \tag{3.23}$$

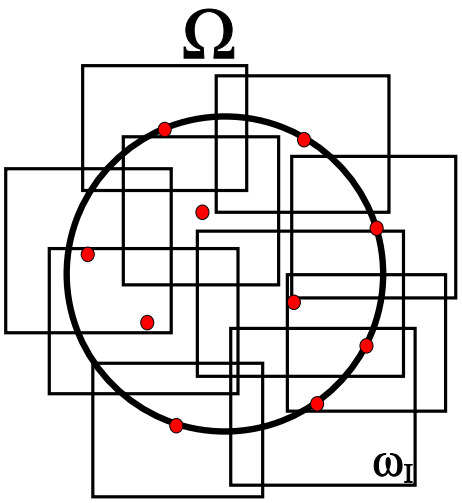

Figure 3.1: *domain covering*

unless the used basis polynomial is capable to approximate $u(\mathbf{x})$ exactly at the particles. Even if the MLS-approximation is usually non-interpolating, it provides nevertheless a very high approximation accuracy in the entire domain Ω.

The MLS-algorithm does generally not underly any restrictions by means of the shape of domain Ω as well as its boundaries. It was shown that also non-convex boundaries and cracks can be dealt with (Organ *et al.* 1996). In the case of cracks, the MLS interpolation function took near the crack a discontinuous shape in order to reassemble the discontinuity of the displacement field at the crack.

3.1.2 Weight function

The weight function Φ or window function in the MLS-approximation scheme (Eq. 3.3) ensures the local character of the approximation around a point of interest $\mathbf{x}$ within a domain Ω by restricting the support of each particle P_I:

$$\Phi\left(\frac{\mathbf{x}-\mathbf{x}_I}{\varrho}\right) = \begin{cases} > 0 & , \quad \mathbf{x} \in supp\{\Phi\} \\ 0 & , \quad \mathbf{x} \notin supp\{\Phi\} \end{cases} , \tag{3.24}$$

where ϱ denotes the influence radius of each particle. This means, each particle $\mathbf{x}_I \in \Omega$ has attached its own support ω_I which is also called domain of influence or influence zones depicted in Fig. 3.1.

In two dimensions the influence zones reassemble discs or rectangles and in three dimensions balls or cuboids. Accordingly, each particle is associated with a shape function (Eq. 3.5), the support of which is the same as for the weight function. The shape functions are overlapping each other so that each point in domain Ω is supported by several particles.

As mentioned before, the local support of each particle plays a crucial role with respect to the accuracy and the stability of the solution, similar as the element size in FEM does. The window function Φ, however, does not only ensure the locality of the approximation, but also its global smoothness in domain Ω. This means that the coefficients $\mathbf{a}$ in (Eq. 3.1) obtained with 1) a constant weight function in the entire domain Ω would be constant over Ω, 2) with a constant weight function having compact support ω_I associated with particles P_I would be piecewise constant over sub-domains $\tilde{\omega} \subset \Omega$ which have the same particle support denoted by the set $\Lambda_{\tilde{\omega}}$:

$$\tilde{\omega} := \left\{ \mathbf{x} \,\middle|\, \mathbf{x} \in \omega_I \ \wedge \ \mathbf{x} \in \omega_J \right\} , \qquad \text{with } I,\, J \in \Lambda_{\tilde{\omega}} \subset \Lambda = const. , \tag{3.25}$$

and 3) a smooth weight function having a compact support ω_I would be a function of $\mathbf{x}$ over the entire domain Ω denoted by $\mathbf{a}(\mathbf{x})$. As a consequence the global approximation $u^h(\mathbf{x})$ would be 1) a linear polynomial fit through the sample points $u(\mathbf{x}_I)$, 2) a piecewise linear polynomial fit through the sample points, or 3) a smooth and continuous approximation of $u(\mathbf{x})$. That is, the local approximation on $\tilde{\omega}$ inherits the smoothness of the weight function (Dolbow and Belytschko 1998).

It was suggested by Liu *et al.* (1997) that the following normalizing rule should be taken into account

$$\int_{-1}^{1}\int_{-1}^{1}\int_{-1}^{1} \Phi(\mathbf{x}) \ dx\, dy\, dz = 1 \tag{3.26}$$

which is equivalent to

$$\int_{-\varrho}^{\varrho}\int_{-\varrho}^{\varrho}\int_{-\varrho}^{\varrho} \frac{1}{\varrho^3} \Phi\left(\frac{\mathbf{x}-\mathbf{x}_I}{\varrho}\right) \ dx\, dy\, dz = 1 \, . \tag{3.27}$$

In three dimensions a weight function with cuboid support ω_I

$$\omega_I := \left\{ \mathbf{x} \in \mathbb{R}^3 \,\middle|\, |x - x_I| \le \varrho_x \wedge |y - y_I| \le \varrho_y \wedge |z - z_I| \le \varrho_z \right\} , \tag{3.28}$$

can be computed as follows (Dolbow and Belytschko 1998)

$$\Phi\left(\frac{\mathbf{x}-\mathbf{x}_I}{\varrho}\right) \equiv w\left(\frac{x-x_I}{\varrho_x}\right) w\left(\frac{y-y_I}{\varrho_y}\right) w\left(\frac{z-z_I}{\varrho_z}\right) . \tag{3.29}$$

The cuboid influence zone has the advantage over the spherical one that its shape can be individually designed with respect to each coordinate direction. This is especially beneficial e.g. for structures which are thin in one or two directions.

The usual choice for the one-dimensional weight-functions w are splines, as they can be specifically designed to meet any desired continuity requirements. This is very beneficial,

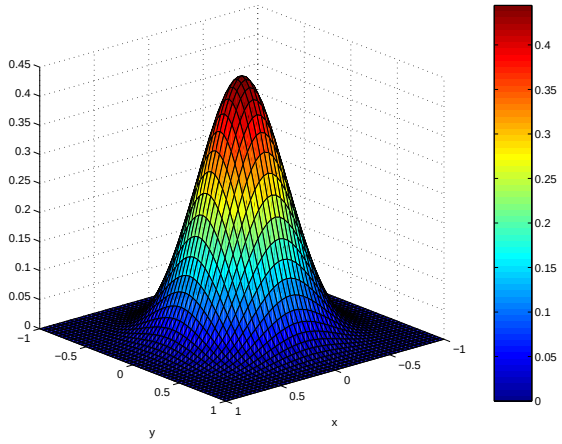

Figure 3.2: *cubic spline* $\Phi = w(x)\, w(y)$

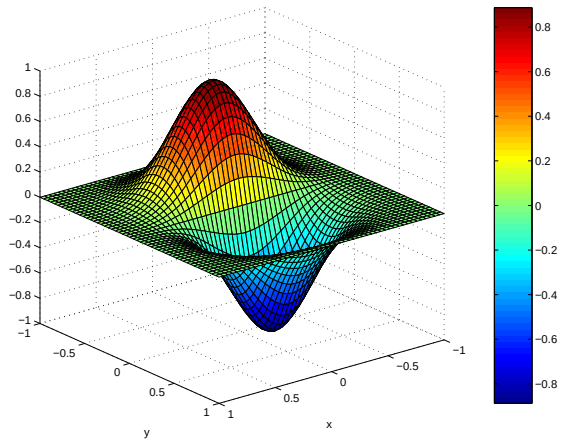

Figure 3.3: *first order derivative of the cubic spline* $\Phi_{,y} = \frac{1}{\varrho}\, w\, w_{,y}(y)$

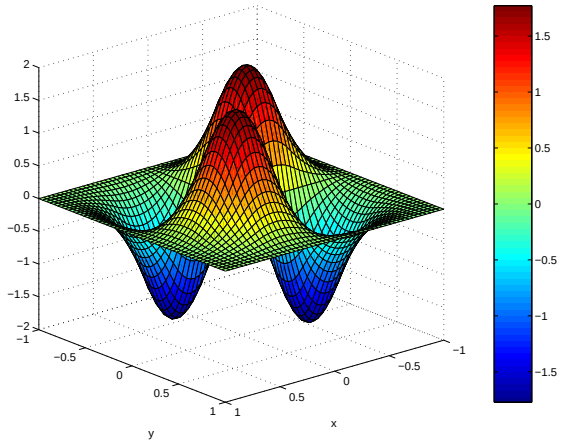

Figure 3.4: *second order derivative of the cubic spline* $\Phi_{,xy} = \frac{1}{\varrho^2}\, w_{,x}(x)\, w_{,y}(y)$

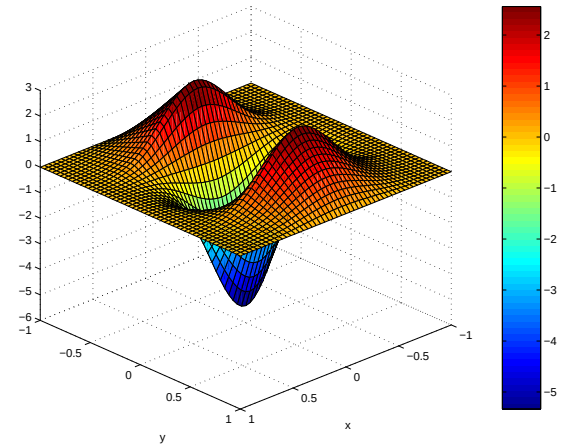

Figure 3.5: *second order derivative of the cubic spline* $\Phi_{,xx} = \frac{1}{\varrho^2}\, w(x)\, w_{,yy}(y)$

because the conventional finite element method fails to provide $C^l(\Omega)$-continuity with $l \geq 1$. In the following, a few splines are presented which were suggested by Liu and Belytschko in various publications and also implemented in the coding of this research project. The illustrations of these splines will be shown as two-dimensional plots.

- The cubic spline defined by

$$w(r) = \begin{cases} \frac{2}{3} - 4r^2 + 4r^3 & \text{for } |r| \leq \frac{1}{2}\,, \\ \frac{4}{3} - 4r + 4r^2 - \frac{4}{3}r^3 & \text{for } \frac{1}{2} < |r| \leq 1\,, \\ 0 & \text{for } |r| > 1\,, \end{cases} \tag{3.30}$$

where $r = (x - x_I)/\varrho$, possesses C^2 -continuity and is illustrated in Fig. 3.2. Its first and second order derivatives are depicted in Fig. 3.3, Fig. 3.4 and Fig. 3.5, respectively.

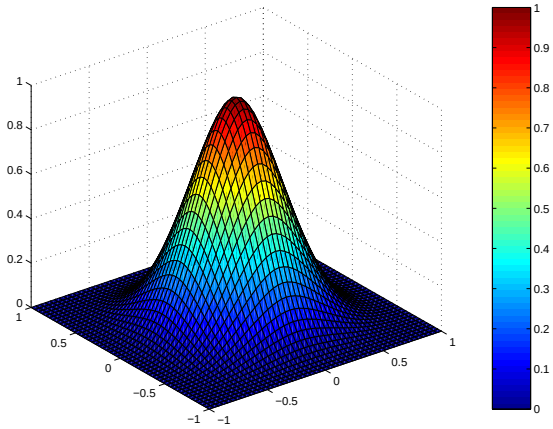

Figure 3.6: *quartic spline* $\Phi = w(x)\, w(y)$

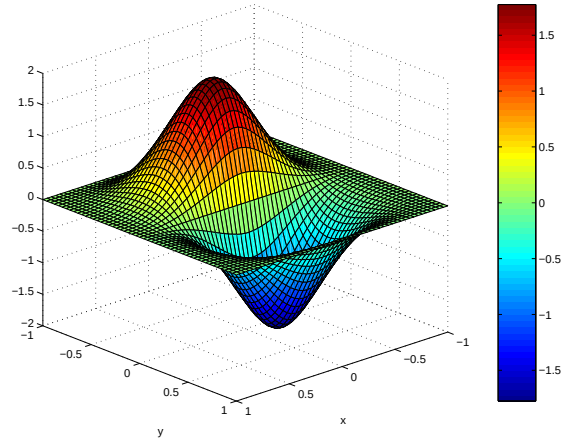

Figure 3.7: *first order derivative of the quartic spline* $\Phi_{,y} = \frac{1}{\varrho}\, w(x)\, w_{,y}(y)$

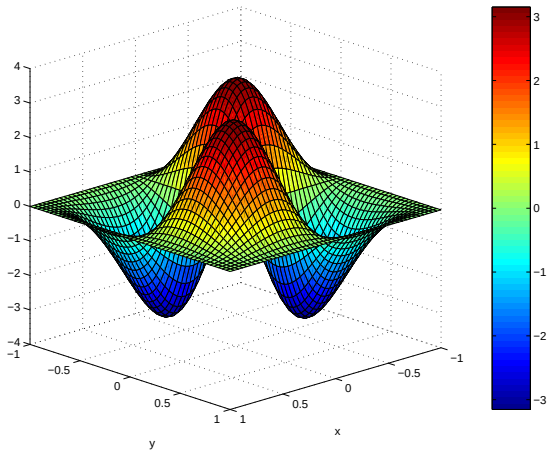

Figure 3.8: *second order derivative of the quartic spline* $\Phi_{,xy} = \frac{1}{\varrho^2}\, w_{,x}(x)\, w_{,y}(y)$

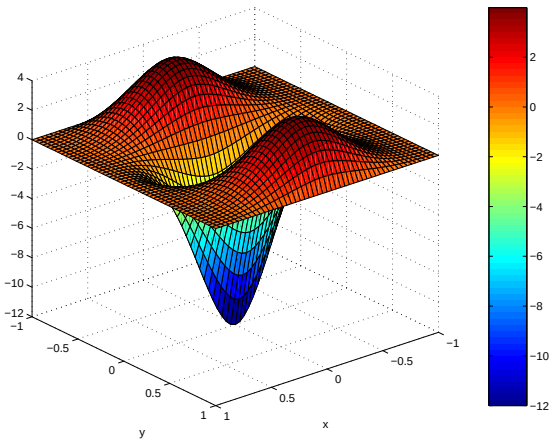

Figure 3.9: *second order derivative of the quartic spline* $\Phi_{,yy} = \frac{1}{\varrho^2}\, w(x)\, w_{,yy}(y)$

- The quartic spline given by

$$w(r) = \begin{cases} 1 - 6r^2 + 8r^3 - 3r^4 & \text{for } |r| \leq 1 \,, \\ 0 & \text{for } |r| > 1 \,, \end{cases} \tag{3.31}$$

  is characterized by C^2-continuity. The quartic spline is displayed in Fig. 3.6 and its first and second derivatives in Fig. 3.7, Fig. 3.8 and Fig. 3.9, respectively.

- The Gaussian spline expressed by

$$w(r) = \begin{cases} e^{-(r/0.4)^2} & \text{for } |r| \leq 1 \,, \\ 0 & \text{for } |r| > 1 \,, \end{cases} \tag{3.32}$$

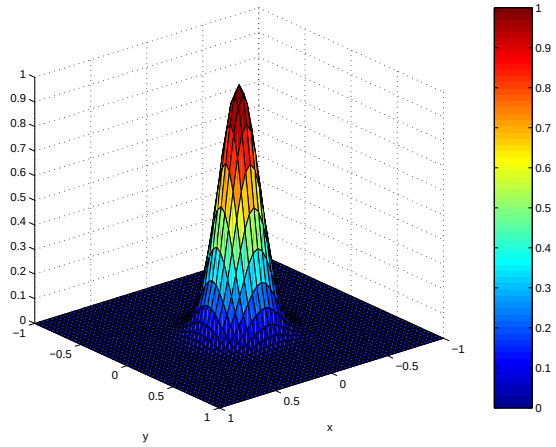

Figure 3.10: *Gaussian spline* $\Phi = w(x)\, w(y)$

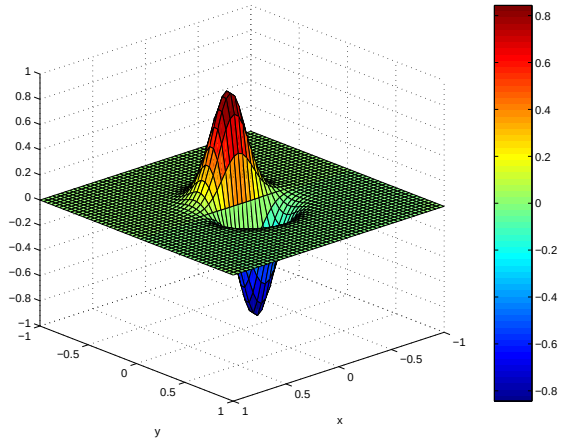

Figure 3.11: *first order derivative of the Gaussian spline* $\Phi_{,y} = \frac{1}{\varrho}\, w(x)\, w_{,y}(y)$

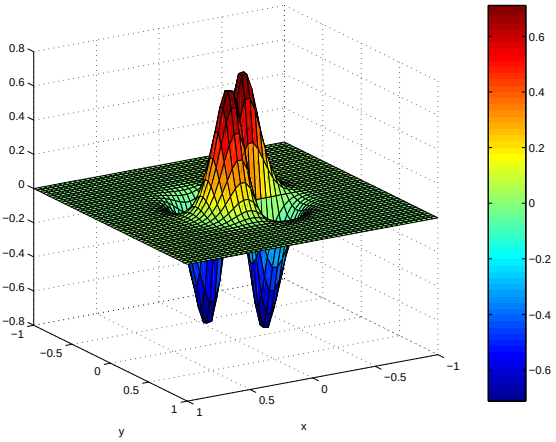

Figure 3.12: *second order derivative of the Gaussian spline* $\Phi_{,xy} = \frac{1}{\varrho^2}\, w_{,x}(x)\, w_{,y}(y)$

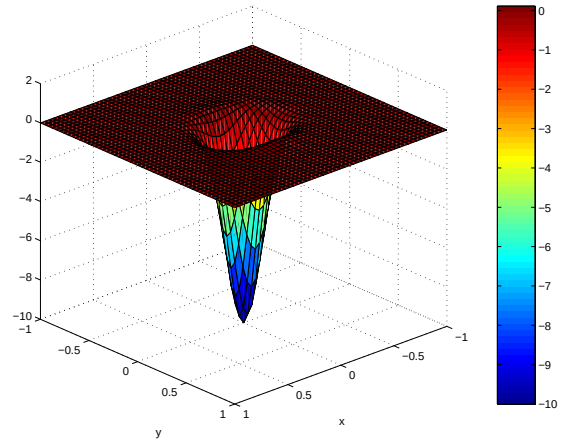

Figure 3.13: *second order derivative of the Gaussian spline* $\Phi_{,yy} = \frac{1}{\varrho^2}\, w(x)\, w_{,yy}(y)$

actually possesses C^{-1}-continuity, because it does not exactly vanish for $|r| = 1$, but takes values which are only numerically equivalent to zero. However, from a numerical perspective the Gaussian spline can be assumed to be C^∞ continuous.

- Another Gaussian spline was introduced in the EFG method (Lu, Belytschko and Gu 1994) which possessed C^∞-continuity

$$w(x - x_I) = \begin{cases} \dfrac{e^{-\left(\frac{x-x_I}{c}\right)^{2k}} - e^{-\left(\frac{\varrho}{c}\right)^{2k}}}{1 - e^{-\left(\frac{\varrho}{c}\right)^{2k}}} & \text{for } x - x_I \le \varrho\,, \\ 0 & \text{for } x - x_I > \varrho\,, \end{cases} \tag{3.33}$$

where parameter $k = 1$ and c were given by

$$c = \alpha\, c_I\,, \qquad \text{with} 1 \leq \alpha \leq 2 \tag{3.34}$$

and c_I was determined individually for each particle x_I as follows

$$c_I = \max_{J \in \Lambda_{c_I}} |x_J - x_I|\,. \tag{3.35}$$

The set of particles Λ_{c_I} was defined by

$$\Lambda_{c_I} \equiv \{J\,|x_I \in \omega_J \ \wedge \ x \in \omega_J\}\,. \tag{3.36}$$

As parameter c is related to the local particle density, this weight function is adaptive to any irregular particle distribution. Parameter α was found best to be chosen close to 1, if singularities and high gradients were to be dealt with. The Gaussian spline, its first derivative and second derivatives are shown in Fig. 3.10, Fig. 3.11, Fig. 3.12 and Fig. 3.13, respectively.

Overall, out of the above selection of splines the MLS scheme provides the best solution approximation using the cubic spline which will be elaborated in Sec. 3.2.

3.1.3 Basis polynomial

As discussed in Sec. 3.1.1 the MLS-algorithm requires a complete polynomial basis to approximate an unknown function $u(\mathbf{x})$ which also involves that a polynomial of certain degree must be reproduced (Eq. 3.9). In fact, the approximation properties of a MLS interpolation is strongly dependent on the used basis polynomial, as the approximation for sub-domains $\tilde{\omega} \subset \Omega$ (Eq. 3.25) which have the same particle support solely relies on the basis polynomial.

In this work three different basis polynomials are used: the Pascal, the Lagrange and the Bernstein polynomial.

- **Pascal polynomial**

  The elements of a polynomial basis of the Pascal type are given by the so-called *Binomian* formulas which are defined by

  $$(x + y + z)^m\,, \tag{3.37}$$

  where m denotes the order of the polynomial. Vector $\mathbf{P}$ which contains the three-dimensional basis polynomial has consequently $l = \frac{1}{6}(m+1)(m+2)(m+3)$ elements.

- **Lagrange polynomial**

  A Lagrange polynomial of m-th order is in one dimension defined as follows

$$P_k(x) = \frac{(x-x_0)(x-x_1)...(x-x_{k-1})(x-x_{k+1})...(x-x_n)}{(x_k-x_0)(x_k-x_1)...(x_k-x_{k-1})(x_k-x_{k+1})...(x_k-x_n)}, \qquad \text{for } k=0,\, m \tag{3.38}$$

  and consists of $l = m+1$ elements. In three dimension we have

$$P_i \equiv P_{IJK} = P_I(x)\, P_J(y)\, P_K(z)\,, \qquad \text{for } I,J,K=0,\, m \tag{3.39}$$

  and vector $\mathbf{P}$ possesses $l = (m+1)^3$ elements.

- **Bernstein polynomial**

  The three-dimensional Bernstein polynomial of order m is given by

$$P_i \equiv P_{IJK} = \left(\begin{array}{c} m \\ I \end{array}\right)\left(\begin{array}{c} m \\ J \end{array}\right)\left(\begin{array}{c} m \\ K \end{array}\right) x(1-x)^{m-I}\, y(1-y)^{m-J}\, z(1-z)^{m-K}\,, \qquad \text{for } I,J,K=0,\, m \tag{3.40}$$

  where

$$\left(\begin{array}{c} m \\ I \end{array}\right) = \frac{m!}{i!\,(m-I)!},$$

  and has got $l = (m+1)^3$ elements.

Other complete polynomials which could also be applied are for e.g. the Serendipity or the Legendre polynomial.

It is also worthwhile noting that the basis does not necessarily need to be a polynomial, but can include any linearly independent functions. It was shown for an example that the modelling of crack propagation (Belytschko *et al.* 1996) benefits from the incorporation of trigonometric functions

$$\mathbf{P}(\mathbf{x}) = \left[1, x, y, z, \sqrt{r}\cos\frac{\theta}{2}, \sqrt{r}\sin\frac{\theta}{2}, \sqrt{r}\sin\frac{\theta}{2}\sin\theta, \sqrt{r}\sin\frac{\theta}{2}, \sqrt{r}\cos\frac{\theta}{2}\sin\theta\right] \tag{3.41}$$

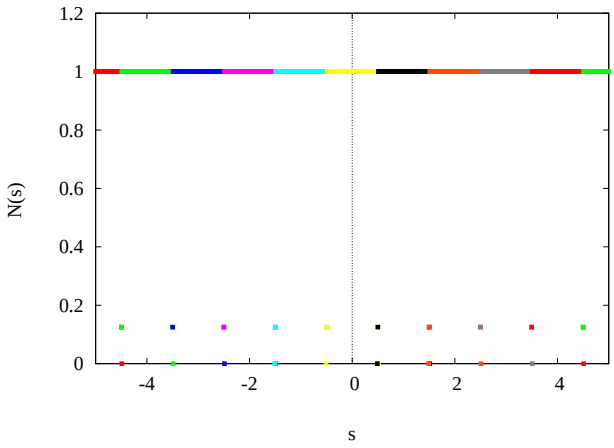

Figure 3.14: *shape function distribution for a zero order basis polynomial* $\varrho = 0.51$

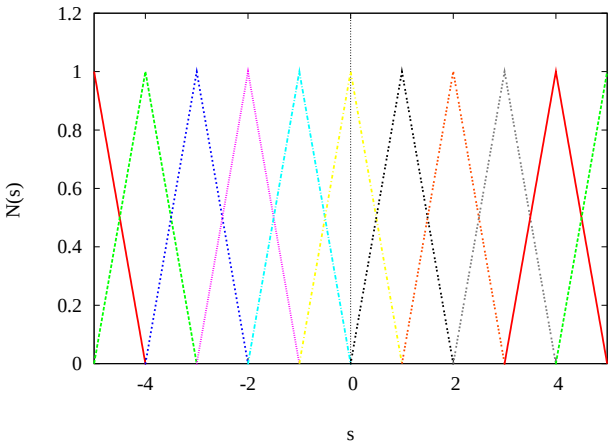

Figure 3.15: *shape function distribution for a first order basis polynomial* $\varrho = 1.01$

3.2 MLS-approximation characteristics

In order to illustrate the characteristics of the MLS approximation scheme in more detail, let us consider a three-dimensional domain

$$\Omega := \left\{ \mathbf{x} \in \mathbb{R}^3 \,|\, x \in [-5,5] \;\wedge\; y \in [-5,5] \;\wedge\; z \in [-5,5] \right\} \tag{3.42}$$

which is discretized by $11 \times 11 \times 11$ equally spaced particles. That is, the particle distance is in each coordinate direction exactly $d = 1.0$. Four different MLS-approximants (Eq. 3.5) shall be distinguished by computing the approximation functions involving a zero order Pascal-type polynomial (Eq. 3.37), its first, second and third order pendant. As weight function the quartic C^3-continuous spline is utilized. Note that in case of the zero order polynomial, which is a constant basis polynomial, we find the analogy to the *Shepard* approximation functions which are used in the *Shepard method* (Eq. 3.7).

The minimum applicable influence radius for the zero order polynomial is determined as $\varrho_{min} > 0.5$. That is, every point of the domain Ω is supported by only one particle, except for the contact plane between two neighbouring influence zones which is supported by two particles. Hence, the shape function of each particle takes the constant value $N(s) = 1.0$ within its support depicted in Fig. 3.14, and correspondingly, its derivatives are zero everywhere. The shape function ordinates $N(s)$ are here and in the following plotted along a line starting from point $(-5, 0, 0)$ and ending at point $(5, 0, 0)$. For the higher order polynomials the minimum influence radius is dictated by the invertibility requirement of the moment matrix (Eq. 3.4) so that the use of the first order polynomial needs at least four supporting particles which is given for $\varrho_{min} > 1.0$, the second order at least ten particles which is provided for $\varrho_{min} > 2.0$, and the third order at least twenty particles which is ensured for $\varrho_{min} > 3.0$. The shape function distribution for the first, second and third order basis polynomial is shown in Fig. 3.15, Fig. 3.16 and Fig. 3.19, respectively. The use of the first order basis polynomial results in a shape function which is not smooth and does accordingly

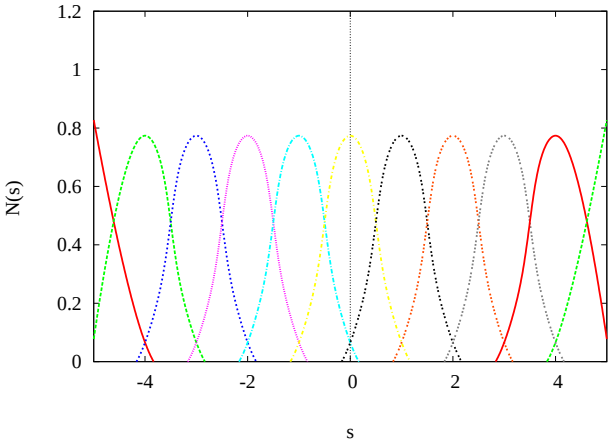

Figure 3.16: *shape function distribution for a second order basis polynomial* $\varrho = 2.01$

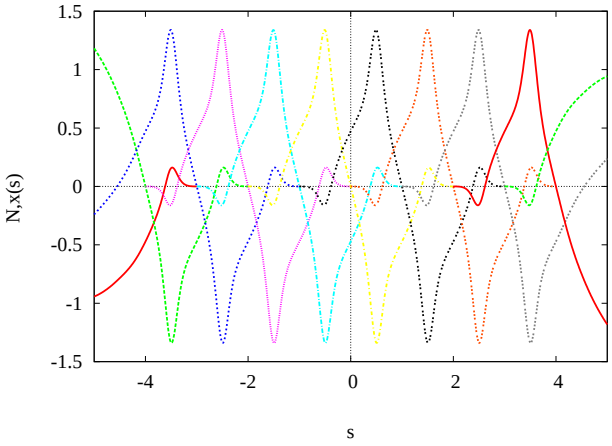

Figure 3.17: *first order shape function derivative distribution for a second order basis polynomial* $\varrho = 2.01$

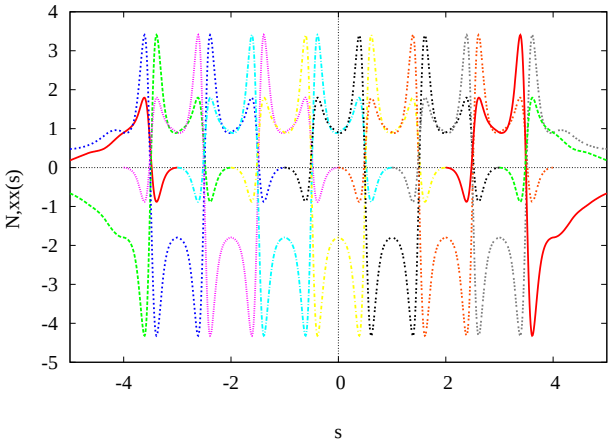

Figure 3.18: *second order shape function derivative distribution for a second order basis polynomial* $\varrho = 2.01$

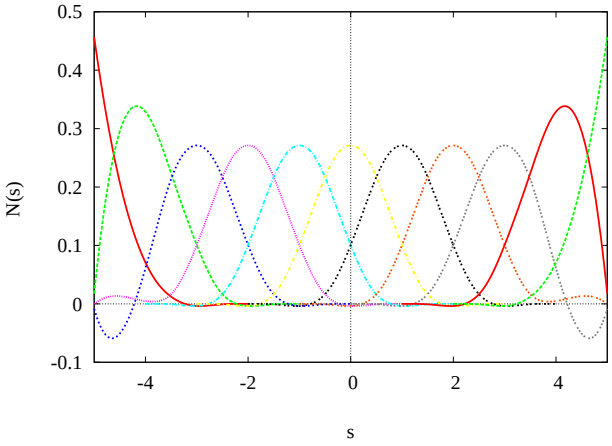

Figure 3.19: *shape function distribution for a third order basis polynomial* $\varrho = 3.01$

not possess continuous first and second derivatives, whereas involving the second or third order basis polynomial results in a smooth shape function and also first order shape function derivative depicted in Fig. 3.17 and Fig. 3.20, respectively. Accordingly, the latter have both a continuous second order derivative illustrated in Fig. 3.18 and Fig. 3.21, respectively. The reason for the non-smoothness of the MLS-approximations functions based on the first order basis polynomial is found in the fact that for $\varrho = 1.01$ only the outskirts of the influence zones are intersecting, where the weight function values are negligible. The overlapping must be therefore of a certain magnitude for numerical reasons. It should be noted that the lack of particle support at boundary makes it necessary that the influence radius of all particles must be chosen larger than actually required for the interior domain. This is especially so when using the second or third order basis polynomial, which also explains the smoothness of the corresponding shape function and its derivatives due to the sufficient overlapping of

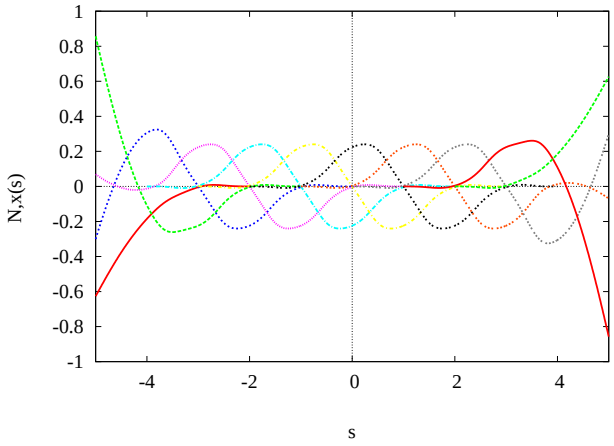

Figure 3.20: *first order shape function derivative distribution for a third order basis polynomial* $\varrho = 3.01$

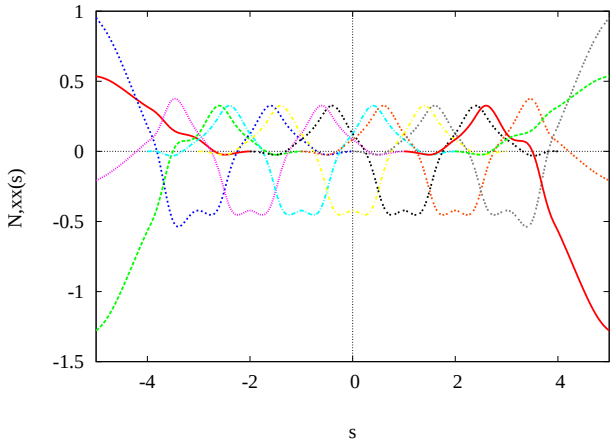

Figure 3.21: *second order shape function derivative distribution for a third order basis polynomial* $\varrho = 3.01$

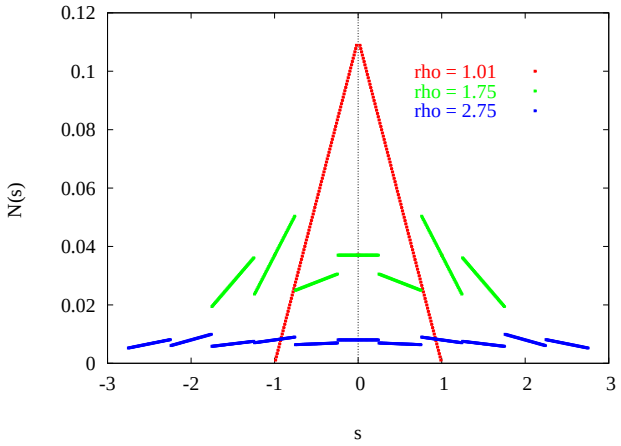

Figure 3.22: *shape function using a first order basis polynomial and a constant weight function for different* ϱ

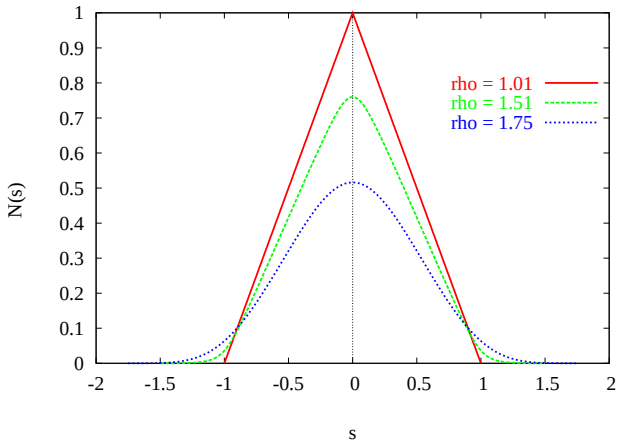

Figure 3.23: *shape function using a first order basis polynomial and the* C^3 *weight function for different* ϱ

the influence zones.

In case of the zero and first order polynomial the minimal applicable influence radius provides that the *Kronecker Delta condition* is fulfilled at each particle. Thus, the shape function ordinates of all neighbouring particles vanish and as MLS is a *partition of unity*, the shape function of the particular particle itself takes the value one. As reason for this characteristic we find that the minimum particle support coincides with the maximum number of sample points which can be exactly approximated by the weighted least square fit (Eq. 3.2). The minimum influence radius determined for the second and third order polynomial however, results in a particle support which is higher than actually required and therefore higher than the used basis polynomial can exactly interpolate. Consequently, they do not hold the *Kronecker Delta property*.

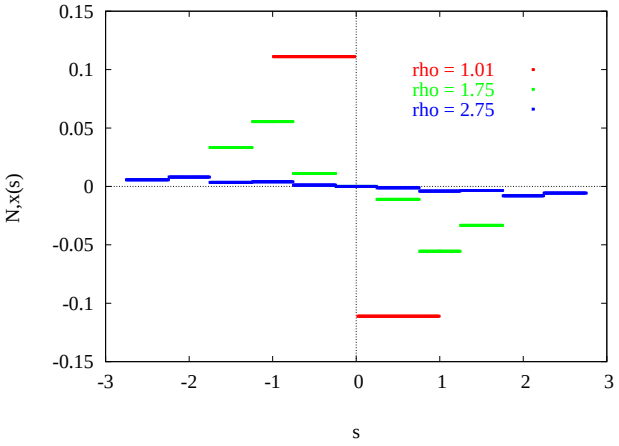

Figure 3.24: *first order shape function derivative using a first order basis polynomial and a constant weight function for different ϱ*

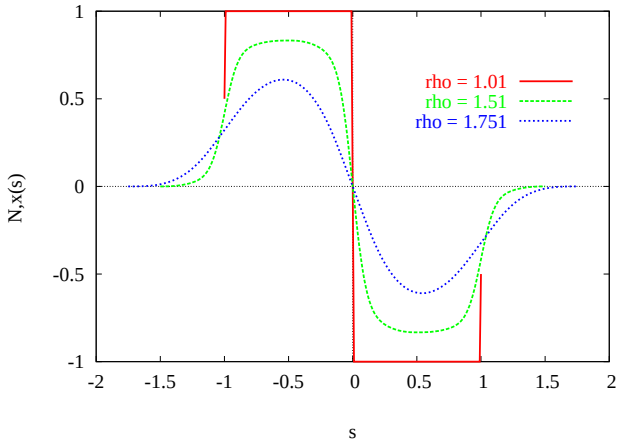

Figure 3.25: *first order shape function derivative using a first order basis polynomial and the C^3 weight function for different ϱ*

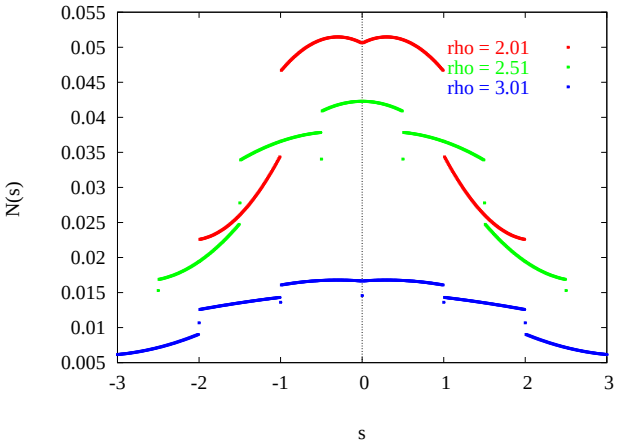

Figure 3.26: *shape function using a second order basis polynomial and a constant weight function for different ϱ*

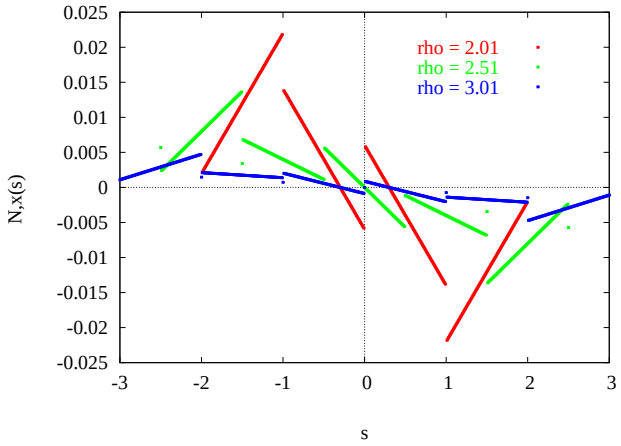

Figure 3.27: *first order shape function derivative using a second order basis polynomial and a constant weight function for different ϱ*

As mentioned before, the smoothness of the shape function and its derivatives requires a certain minimum overlapping of the support zones, otherwise the involved weight function ordinates are numerically too small. The regularity of MLS-approximation functions however, is also dependent on the overlapping. This is clear as the MLS-shape function is with a constant weight function only piecewise continuous in sub-domains $\tilde{\omega} \subset \Omega$ (Eq. 3.25) which have the same particle support. Accordingly, the discontinuities between those sub-domains have to be closed by the weight function. Furthermore, MLS is a *partition of unity* (Eq. 3.10) so that a higher particle support means a smaller magnitude of each of the corresponding shape function ordinates of the involved particles and consequently, of the discontinuities which have to be bridged. This fact is illustrated in Fig. 3.22 for the MLS-shape function of

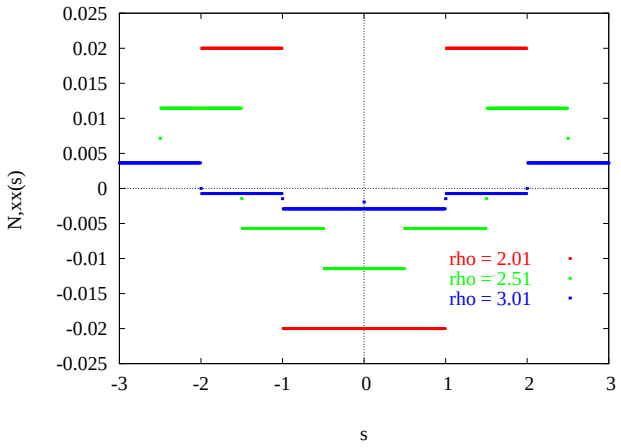

Figure 3.28: *second order shape function derivative using a second order basis polynomial and a constant weight function for different ϱ*

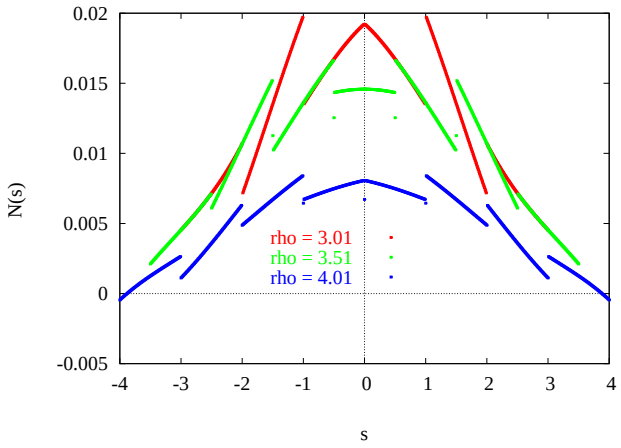

Figure 3.29: *shape function using a third order basis polynomial and a constant weight function for different ϱ*

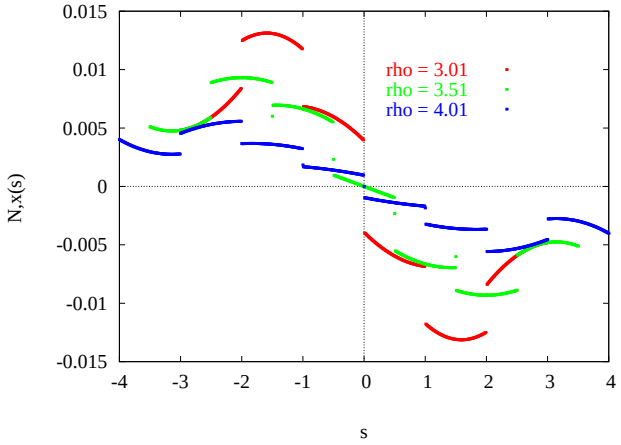

Figure 3.30: *first order shape function derivative using a third order basis polynomial and a constant weight function for different ϱ*

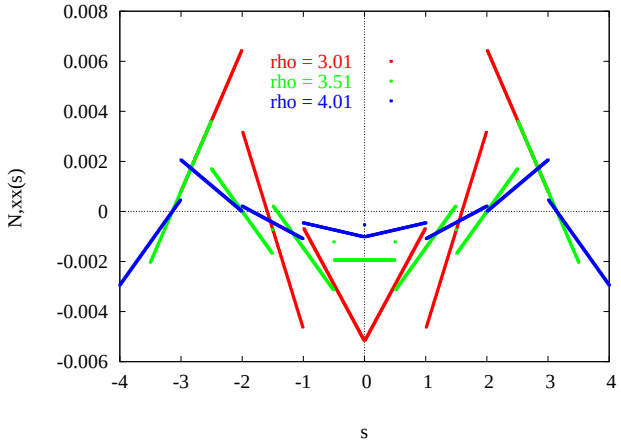

Figure 3.31: *second order shape function derivative using a third order basis polynomial and a constant weight function for different ϱ*

the particle which is in the center of domain Ω making use of the first order basis polynomial and a constant weight function $\Phi = 1.0$. Correspondingly, the use of the C^3-continuous quartic spline introduced in App. A exhibits a different level of smoothness and regularity depicted in Fig. 3.23. Furthermore, a higher density of sub-domains $\tilde{\omega}$ within a single influence zone ω_I further reduces the discontinuities between the sub-domains $\tilde{\omega}$ which is clearly visible for the shape function and its first order derivatives shown in Fig. 3.22 and 3.24. The same applies using the second and third order basis polynomial, where a larger particle influence radius reduces the discontinuity gap of the shape function, its first and second order derivatives as displayed in Fig. 3.26 - Fig. 3.31. It can be therefore summarized that a certain minimum amount of overlapping of the influence zones is necessary, however,

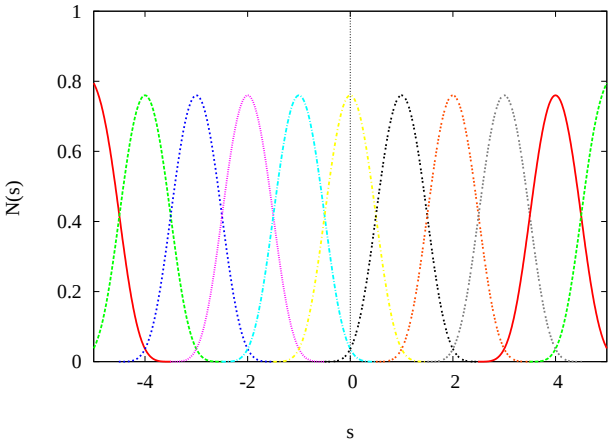

Figure 3.32: *shape function distribution for a zero order basis polynomial* $\varrho = 1.51$

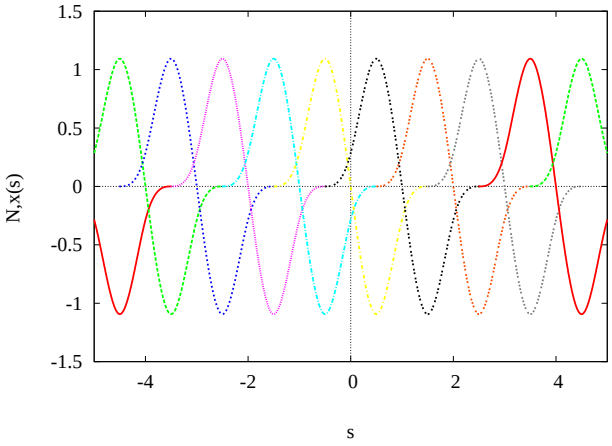

Figure 3.33: *first order shape function derivative distribution for a zero order basis polynomial* $\varrho = 1.51$

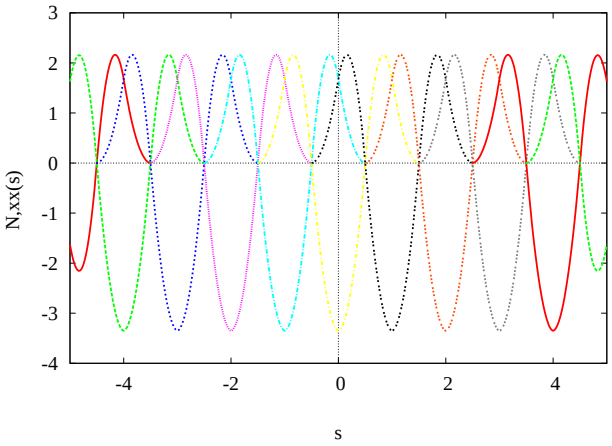

Figure 3.34: *second order shape function derivative distribution for a zero order basis polynomial* $\varrho = 1.51$

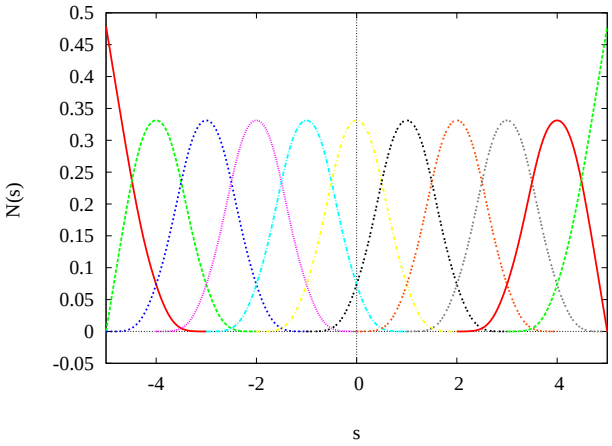

Figure 3.35: *shape function distribution for a first order basis polynomial* $\varrho = 1.75$

at the same time the approximation locality should be preserved, i.e. the minimal needed particle support should not be exceeded too much. Thus, there should be an optimal influence radius for which the maximization of the approximation locality on the one hand and the minimization of the discontinuity gaps between continuous parts of the shape function as well as its derivatives on the other hand is in balance. This assumption will be confirmed in the latter.

Now, a smooth and regularly formed shape function with a distinct maximum is achieved in case of the zero order basis polynomial for $\varrho_{min} = 1.51$ and the first order polynomial for $\varrho_{min} = 1.75$ depicted in Fig. 3.32 and Fig. 3.35, respectively. Accordingly, the smoothness of both shape functions provides that their first and second order derivatives are continuous too, shown in Fig. 3.33 and Fig. 3.34 as well as in Fig. 3.36 and Fig. 3.37, respectively.

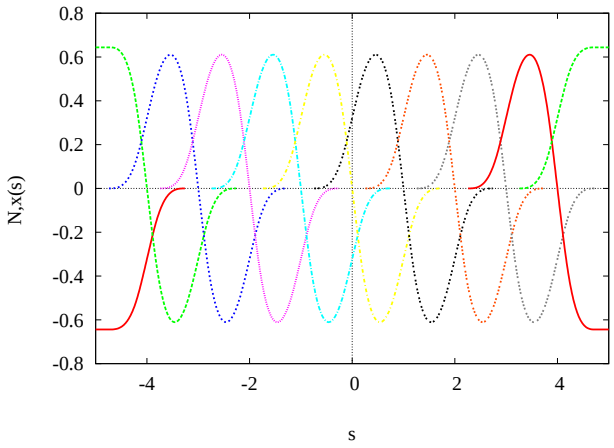

Figure 3.36: *first order shape function derivative distribution for a first order basis polynomial* $\varrho = 1.75$

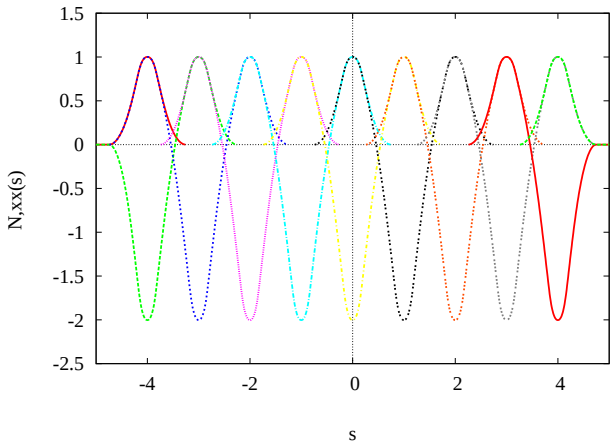

Figure 3.37: *second order shape function derivative distribution for a first order basis polynomial* $\varrho = 1.75$

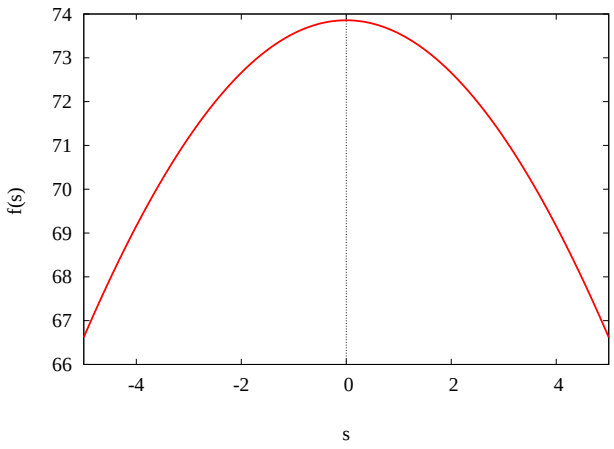

Figure 3.38: *function based on a tenth-order polynomial*

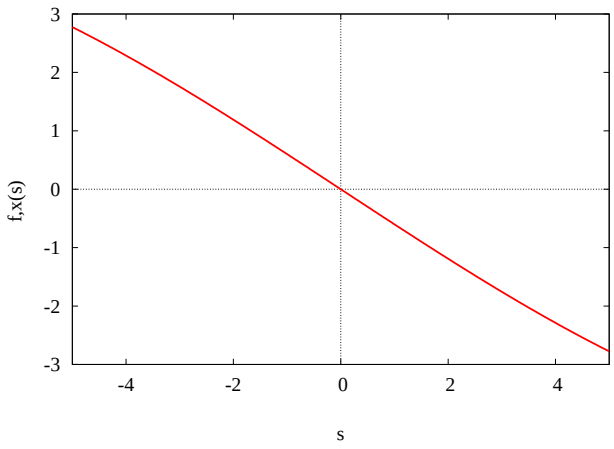

Figure 3.39: *first order derivative of the function based on tenth-order polynomial*

In the following the dependency of the approximation accuracy on the used weight function and basis polynomial will be investigated. Furthermore, it will be demonstrated that the optimal influence radius, which provides the best accuracy, is not necessarily the minimal applicable. For this, we consider a function defined in the domain Ω (Eq. 3.42) which is constructed by a tenth order polynomial as follows

$$f(\tilde{\mathbf{x}}) = 100\,(1-\tilde{x}^2)^5\,(1.0-\tilde{y}^2)^5\,(1.0-\tilde{z}^2)^5\,, \qquad \text{with } \tilde{\mathbf{x}} = \frac{1}{35}\,\mathbf{x}\,. \tag{3.43}$$

This function and its derivatives $\frac{\partial f}{\partial x}$ and $\frac{\partial^2 f}{\partial x \partial x}$ are illustrated in Fig. 3.38, Fig. 3.39 and Fig. 3.40, respectively, which are plots along a line starting from point $(-5, 0, 0)$ and ending at point $(5, 0, 0)$. This function and its derivatives shall now be approximated by different MLS-approximations computed with the Pascal-type polynomial (Eq. 3.37) of zero, first,

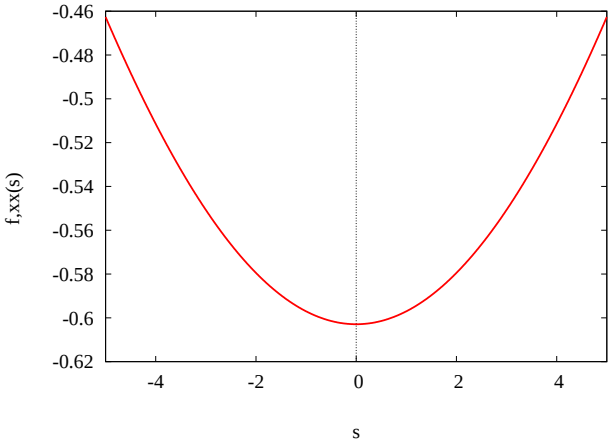

Figure 3.40: *second order derivative of the function based on a tenth-order polynomial*

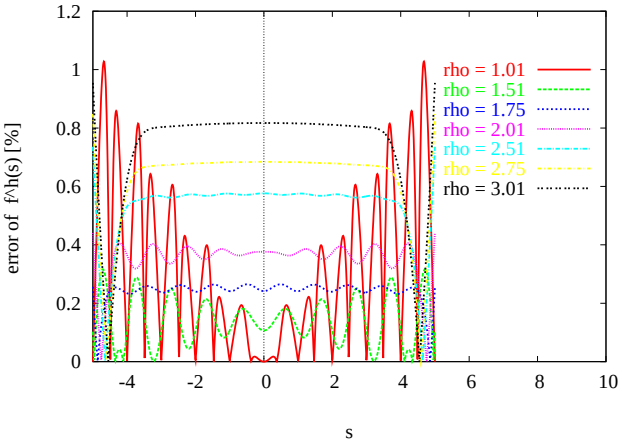

Figure 3.41: *MLS-approximation of a tenth-order polynomial using a zero order basis polynomial for various ϱ*

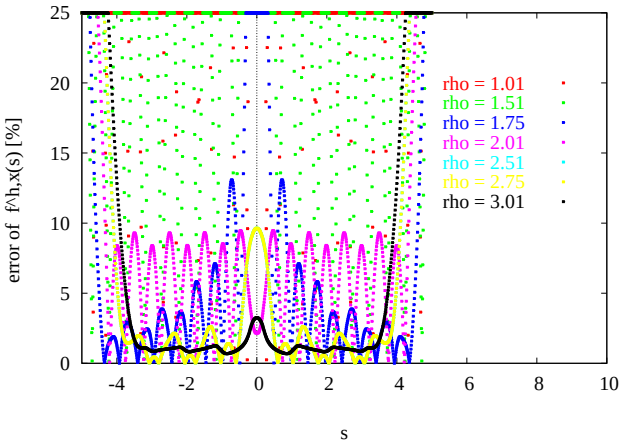

Figure 3.42: *MLS-approximation of the first order derivative of a tenth-order polynomial using a zero order basis polynomial for various ϱ*

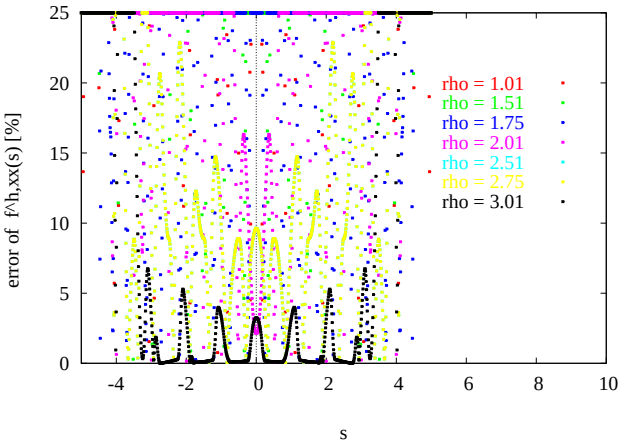

Figure 3.43: *MLS-approximation of the second order derivative using a tenth-order polynomial using a zero order basis polynomial for various ϱ*

second and third order as well as various values for the influence radius ϱ. Note that the same ϱ is always applied to all particles in the domain Ω. The error, which is the ratio of the approximation to the exact value of the function and its derivatives, will be displayed along the same plotting line as the function before. Error values which are beyond 25 % will be cut off.

Using the zero order polynomial and setting $\varrho = 0.51$ the MLS-approximation depicted in Fig. 3.41 is very accurate at the particles as expected, considering that the MLS-approximation holds the *Kronecker Delta condition* at the particles as shown in Fig. 3.14. The same applies for the first order polynomial, when we use $\varrho = 1.01$ shown in Fig. 3.44, as the shape functions also hold the *Kronecker Delta condition* as depicted in Fig. 3.15. The

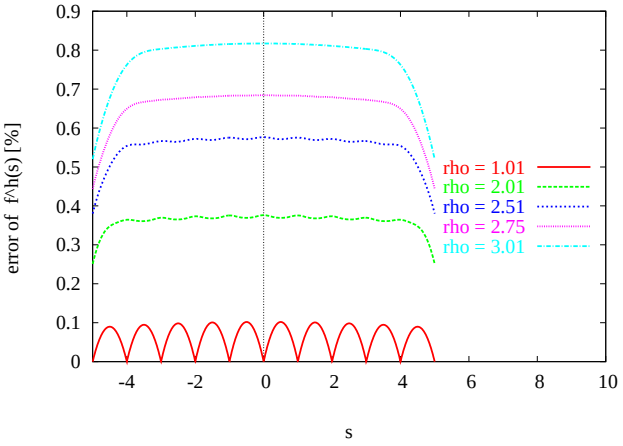

Figure 3.44: *MLS-approximation of a tenth-order polynomial using a first order basis polynomial for various ϱ*

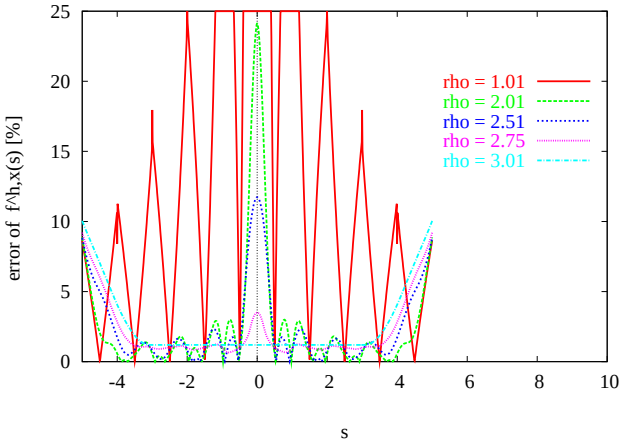

Figure 3.45: *MLS-approximation of the first order derivative of a tenth-order polynomial using a first order basis polynomial for various ϱ*

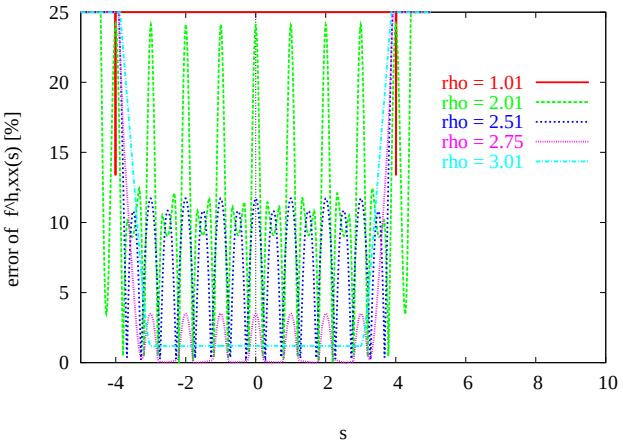

Figure 3.46: *MLS-approximation of the second order derivative of a tenth-order polynomial using a first order basis polynomial for various ϱ*

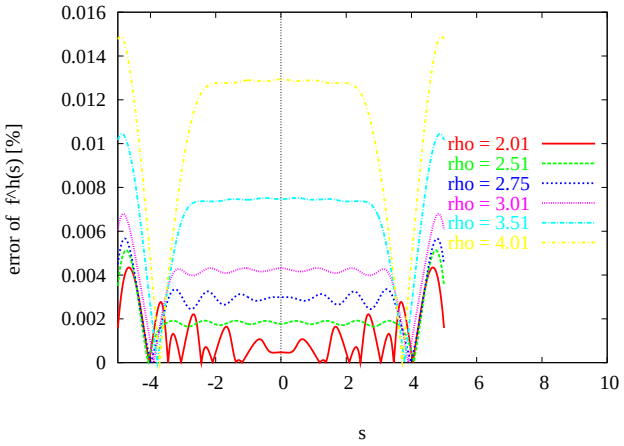

Figure 3.47: *MLS-approximation of a tenth-order polynomial using a second order basis polynomial for various ϱ*

first order and second order derivatives though, are in case of the zero order basis polynomial most accurately approximated for $\varrho = 3.0$ illustrated in Fig. 3.42 and Fig. 3.43. However, at the boundary the error lies for both beyond 25 %. Utilizing the first order polynomial, the optimal influence radius is determined as $\varrho = 2.75$ to achieve to best MLS-approximation of the first and second order derivative of the investigated function depicted in Fig. 3.45 and Fig. 3.46. Again, the error at boundary is considerably higher than within the domain, but the error of the first order derivative is significantly lower than computed with the zero order polynomial. Using the second or the third order basis polynomial we achieve the best approximation of the function for an influence radius $\varrho = 2.01$ and $\varrho = 3.01$, respectively, displayed in Fig. 3.47 and Fig. 3.50 which is the smallest possible one. This is clear, as it

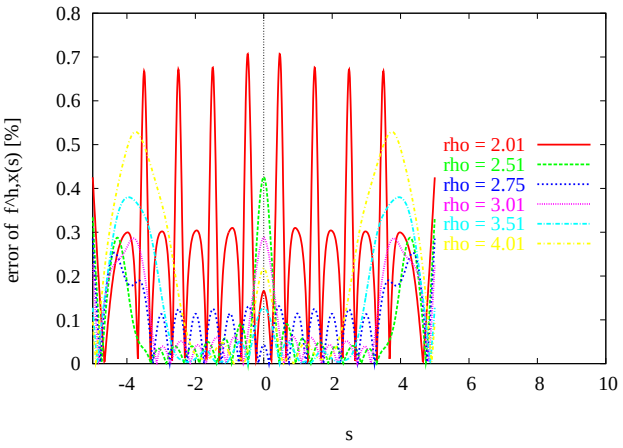

Figure 3.48: *MLS-approximation of the first order derivative of a tenth-order polynomial using a second order basis polynomial for various ϱ*

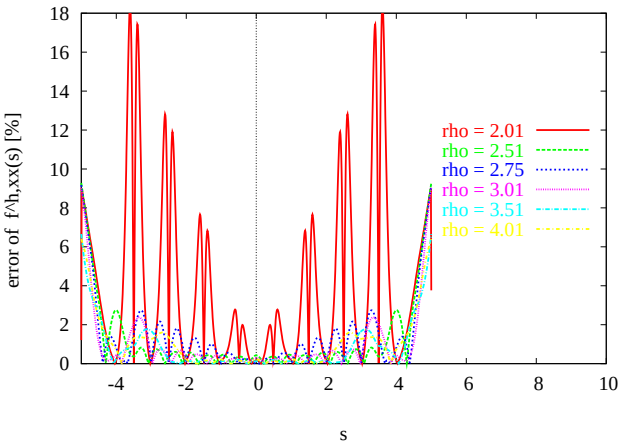

Figure 3.49: *MLS-approximation of the second order derivative using a tenth-order polynomial using a second order basis polynomial for various ϱ*

ϱ	supporting particles
0.51	1 - 2
1.01	18 - 27
1.51	18 - 36
2.01	75 - 125
2.51	75 - 150
2.75	75 - 150
3.01	196 - 343
3.51	196 - 392
4.01	405 - 729

Table 3.1: *particle support distribution for various ϱ*

follows the principle that the more local the approximation, the more accurate it is. For the function derivatives however, the best choice of the influence radius is somewhat indifferent. That is, in case of the second order basis polynomial $\varrho = 3.01$ gives a good approximation for the first and second order derivative depicted in Fig. 3.48 and Fig. 3.49, respectively, except for the second order derivative at boundary, where $\varrho = 2.01$ provides a better result. In case of the third order basis polynomial no clear choice is possible for the first and second order function derivative shown in Fig. 3.51 and Fig. 3.52. However, the boundary approximation accuracy lacks the most for $\varrho = 3.01$.

In the Tab. 3.1 the number of supporting particles are listed for different choices of the influence radius. The minimum particle support is always found at $s = -5$ and $s = 5$ and

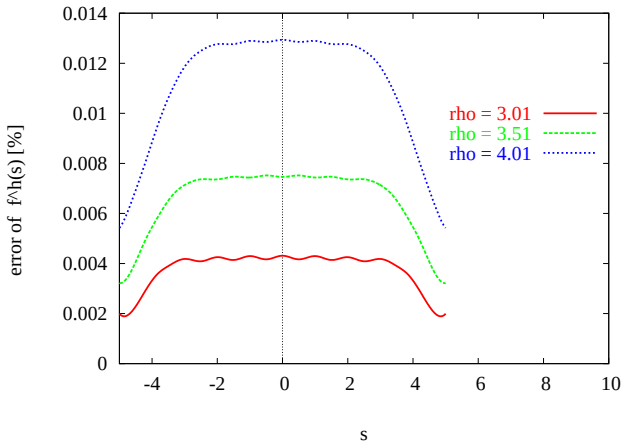

Figure 3.50: *MLS-approximation of a tenth-order polynomial using a third order basis polynomial for various ϱ*

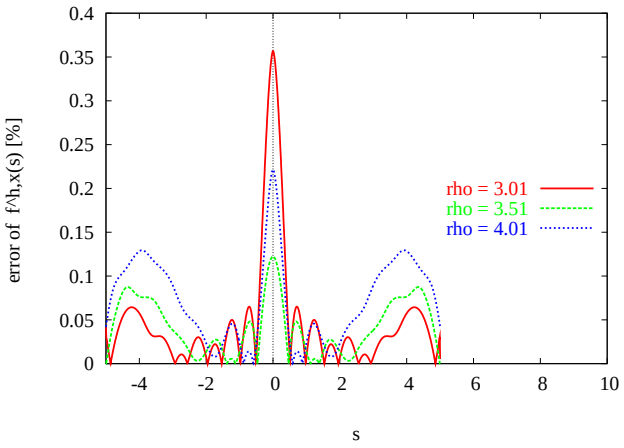

Figure 3.51: *MLS-approximation of the first order derivative of a tenth-order polynomial using a third order basis polynomial for various ϱ*

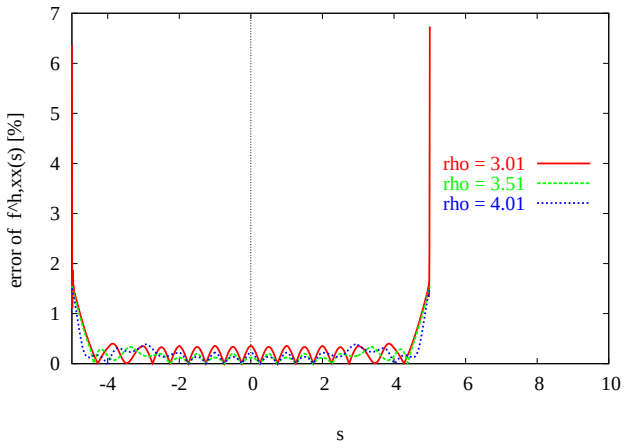

Figure 3.52: *MLS-approximation of the second order derivative of a tenth-order polynomial using a third order basis polynomial for various ϱ*

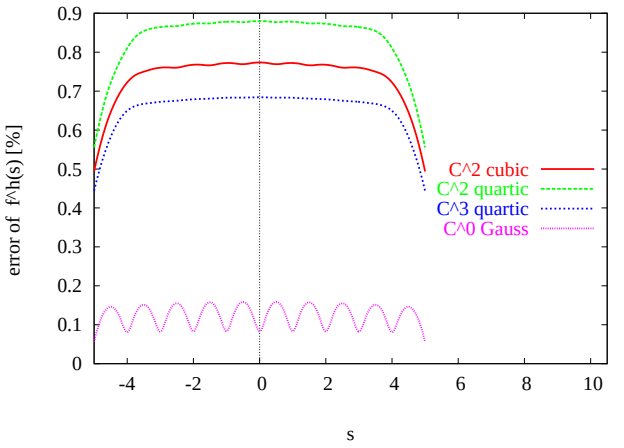

Figure 3.53: *MLS-approximation of a tenth-order polynomial using a first order basis polynomial for various spline weight functions with $\varrho = 2.51$*

the maximum support in the interior domain. Obviously, an influence radius $\varrho > 2.75$ can not be considered to be practical anymore, as the particle support goes beyond 200.

Finally, it is of interest what influence the weight function has on the approximation accuracy. For this, four different weight functions are taken under consideration: these are the cubic spline (Eq. 3.30), the C^2 continuous quartic spline (Eq. 3.31), the C^3-continuous quartic spline presented in App. A and the C^{-1}-continuous Gauss spline (Eq. 3.32). Note that the Gauss spline takes very small numbers at the outskirts of its definition space which are numerically equivalent to zero. Therefore, it is assumed to be C^∞ from the numerical point of view. Now, the MLS-approximation of the function based on the tenth order spline

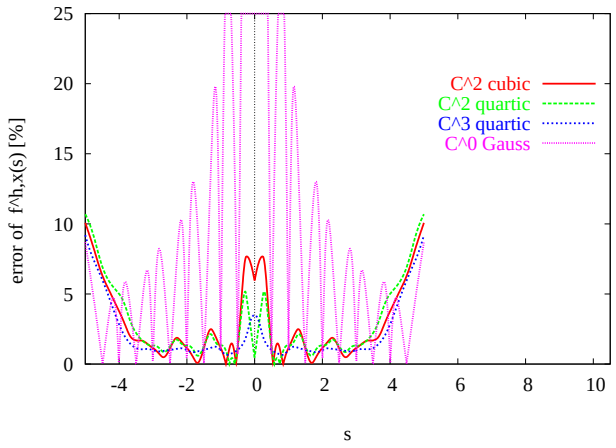

Figure 3.54: *MLS-approximation of the first order derivative of a tenth-order polynomial using a first order basis polynomial for various spline weight functions with* $\varrho = 2.51$

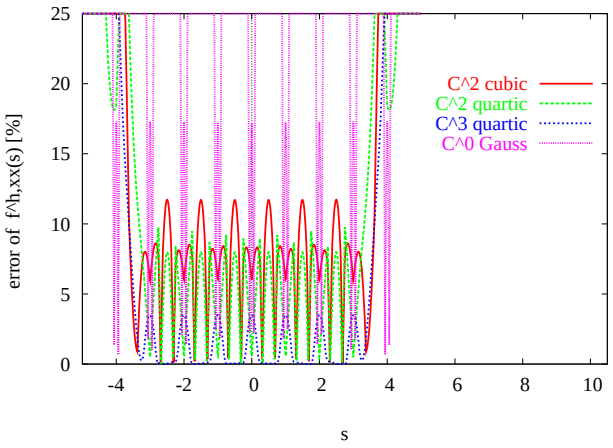

Figure 3.55: *MLS-approximation of the second order derivative using a tenth-order polynomial using a first order basis polynomial for various spline weight functions with* $\varrho = 2.51$

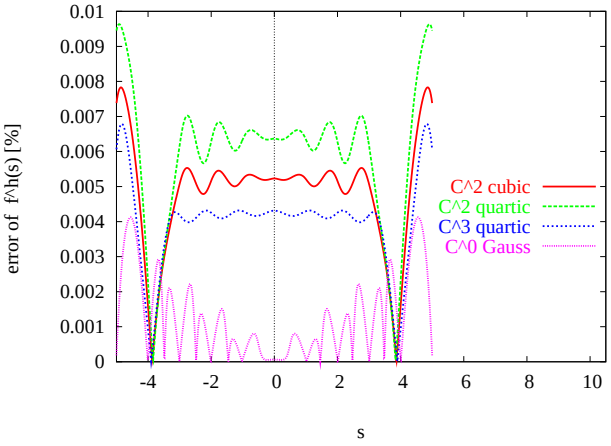

Figure 3.56: *MLS-approximation of a tenth-order polynomial using a second order basis polynomial for various spline weight functions with* $\varrho = 3.01$

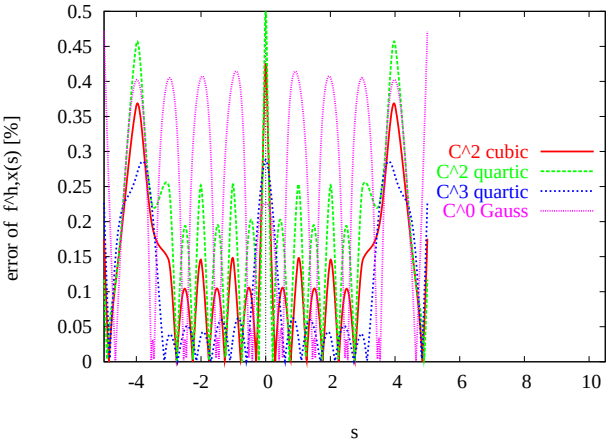

Figure 3.57: *MLS-approximation of the first order derivative of a tenth-order polynomial using a second order basis polynomial for various spline weight functions with* $\varrho = 3.01$

shows an error distribution which is decreasing with the increase of the weight function continuity as displayed in Fig. 3.53, Fig. 3.56 and Fig. 3.59. However, for the approximation of the function derivatives, the numerical continuity of the Gauss spline is obviously not quite sufficient anymore as depicted in Fig. 3.54, Fig. 3.55, Fig. 3.57, Fig. 3.58, Fig. 3.60 and Fig. 3.61, because the use of the cubic spline and also of both quartic splines results in a better approximation. The approximation error of the function and its first and second order derivatives clearly indicates that the C^3-continuous quartic spline is superior in comparison

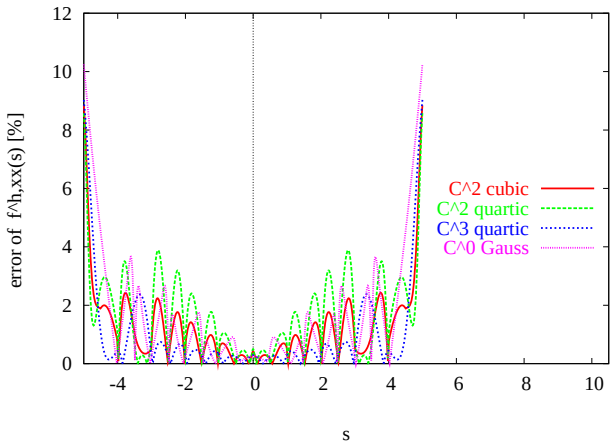

Figure 3.58: *MLS-approximation of the second order derivative using a tenth-order polynomial using a second order basis polynomial for various spline weight functions with* $\varrho = 3.01$

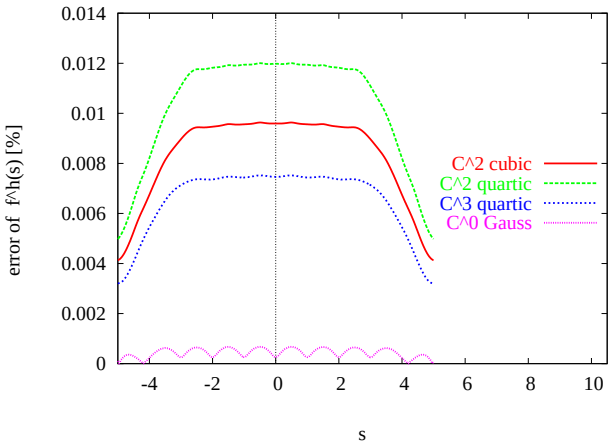

Figure 3.59: *MLS-approximation of a tenth-order polynomial using a third order basis polynomial for various spline weight functions with* $\varrho = 3.51$

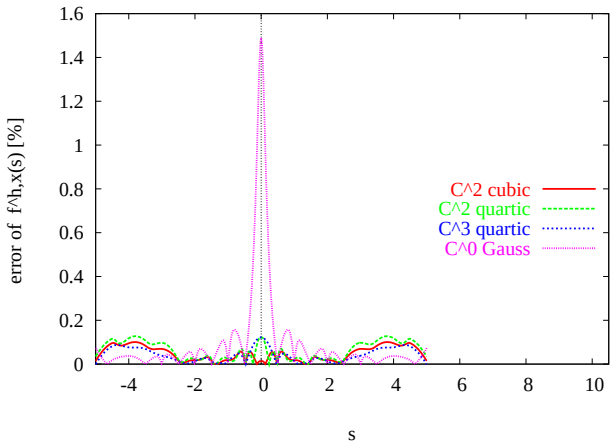

Figure 3.60: *MLS-approximation of the first order derivative of a tenth-order polynomial using a third order basis polynomial for various spline weight functions with* $\varrho = 3.51$

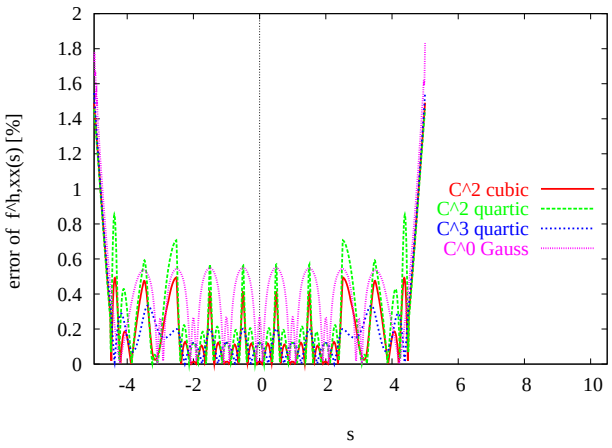

Figure 3.61: *MLS-approximation of the second order derivative of a tenth-order polynomial using a third order basis polynomial for various spline weight functions with* $\varrho = 3.51$

to the cubic and the C^2-continuous quartic spline.

Summarizing, the minimal possible influence radius provides good approximation results for the function itself, but not for its derivatives. It seems that the reduction of the discontinuities between the sub-domains $\tilde{\omega}$ (Eq. 3.25) displayed in Fig. 3.22 - Fig. 3.31 achieved by enlarging the particle influence radius is of greater benefit for the shape function derivatives than for the shape function itself. Correspondingly, when dealing with problems which involve higher order derivatives, the choice of the influence radius has to accommodate both,

the accuracy needed of the function as well as its derivatives. This obviously stands in contradiction, because the approximation accuracy of the function itself is best for the minimal usable ϱ. Therefore, the optimal influence radius is usually not the minimally applicable one, but also not much larger. For an irregular particle distribution the exact value of ϱ can not be predicted anymore, but has to be determined for each particle individually.

Furthermore, the approximation accuracy is increasing with the order of the used basis polynomial and the continuity of the weight function. This is clear as the global continuity of the meshfree approximants in a domain Ω is given by $min(C^l, C^m)$, where the basis polynomial $\mathbf{P} \in C^m(\Omega)$ and the weight function $\Phi \in C^l(\Omega)$ (Lancaster and Salkauskas 1981). Note that the approximation quality of a function and its derivatives within the sub-domains $\tilde{\omega}$, which have a constant particle support, solely depends on the used basis polynomial. Nonetheless, the global approximation is also strongly influenced by the smoothness of the weight function, as it ensures the continuity between those local sub-domains. However, higher order polynomials need a far larger particle support, and therefore amplify the computational costs. A known phenomenon is also that the use of higher order polynomials results in an oscillating solution and spurious modes. Thus, the application of polynomials higher than second order are not found to be practical within this work. Even more so, as the difference in approximation accuracy between second and third order is not very substantial. This shows that the accuracy gain induced by the higher order polynomial is again consumed by the loss of locality due to the larger particle influence zones.

Finally, the approximation accuracy of the function derivatives at the boundary is significantly worse than for the interior domain. In order to decrease the approximation error at boundary, a denser particle distribution in these areas must be applied. For more details the reader is also referred to Sec. 4.3.1, where the boundary approximation accuracy is studied. Furthermore, in Sec. 6.3.3 it is found that especially the symmetry boundary needs a higher particle distribution density in order to achieve an accurate stress field at the boundary.

3.3 Details of a MLS implementation

Generally, there are three major differences between a MLS-based meshfree method and FEM. Firstly, the problem formulation is implemented in global coordinates, i.e. the approximation of the solution function $u^h(\mathbf{x})$ is expressed in global coordinates. Secondly, the numerical integration over the problem domain Ω provides at each integration point not only entries of the discrete equation system that are related to direct neighbour particles of this integration point, but also to neighbour particles which are more distant. This is as each particle usually does not only influence its direct neighbour particles which may be seen as its first layer of surrounding particles, but also its second and sometimes even its third layer. Thirdly, the essential boundary conditions cannot be imposed as easily as in FEM. This is clear recalling that meshfree interpolation functions (Eq. 3.5) do not fulfill the *Kronecker Delta condition*

$$N_I(\mathbf{x}_J) \neq \delta_{IJ} \tag{3.44}$$

unless the weight functions are singular at the particles. Therefore, the particle parameters u_I are not equal to its degrees of freedom. It was proposed by Lancaster and Salkaukas (1981) to avoid this dilemma making use of singular weight functions so that the MLS shape functions are interpolating at the boundary particles. In practise however, it was discovered that the approximation convergence was rather poor (Cheng and Wang 2000).

The basic procedure computing the discrete equation system is comparable between MLS-based meshfree method and FEM. In the following sub-sections implementational issues will be addressed such as the numerical integration and the essential boundary condition enforcement. Notes on the parallelization of the meshfree code which enables it to be run on a distributed memory architecture supercomputer are given in App. B.

3.3.1 Numerical integration

In opposition to meshfree methods which utilize a point collocation approach, most *meshfree Galerkin methods* such as DEM, EFGM, RKPM, hp-cloud, PUM and NEM can not be called truly meshfree, because of their need for a background mesh or background cells to perform the numerical integration over the problem domain. In particular, if the geometry within these cells is separately approximated e.g. by FEM approximants so that in case of the Gauss quadrature the integration point coordinates and weights can be determined, the meshfree method is not purely meshfree anymore. Therefore, some authors considered methods which do not require an extra background mesh such as LBIE (Atluri and Zhu, 2000a), MLPG (Atluri and Zhu, 2000b) and the finite sphere method (De and Bathe, 2000), where the numerical integration is applied on the particle support patches. Alternatively, the use of a particle integration scheme (Beissel and Belytschko 1996; Chen et al. 2001; De and Bathe 2001) frees the meshfree method from an underlying grid. However, none of these methods can be seen as ultima ratio which will be addressed in the following.

Three numerical integration schemes can be distinguished which are commonly applied.

3.3.1.1 Gauss-Legendre quadrature

Before alternative integration methods will be described, the *Gauss-Legendre quadrature* and its implications, when applied to meshfree methods, is outlined. Note that the majority of meshfree methods use the *Gauss-Legendre quadrature* to integrate over the problem domain. For this, a background mesh is laid over the domain and the quadrature has to be performed separately within each cell. That is, a suitable grid has to be found which usually covers the domain exactly. Furthermore, the integration points and their weights have to be determined. If the background grid is taken to be a FEM mesh, simple finite element shape functions can be utilized to approximate the geometry and to obtain coordinates and weights of the integration points. In case of a problem given in the Lagrangian form the approximation of the geometry via FEM is not a serious drawback. However, this integration scheme causes, especially applied to MLS-based meshfree methods, integration errors which lead to a reduced accuracy of the solution. Breitkopf and his co-corkers (2002) as well as De and Bathe (2000)

found that this were due to the non-polynomial character of the meshless approximants. Dolbow and Belytschko (1999) though made the misalignment between particle support zones and integration cells responsible for reduced numerical integration accuracy. Especially the spherical particle influence zone was claimed to be disadvantageous. Therefore, they proposed a so-called bounding box technique to match particle support with background mesh and so to improve the performance of the integration.

3.3.1.2 Gauss-Chebyshev quadrature

As mentioned above the rational character of the MLS-type shape functions suggests the use of a more suitable numerical integration scheme. In case of the finite sphere method the lens shaped integration cell was the cause of a further deterioration of integration accuracy (De and Bathe 2001). Therefore, the authors proposed the usage of the so-called *Gauss-Chebyshev quadrature*, where in contrast to the *Gauss-Legendre quadrature* the use of spherical coordinates allows to determine the integration coordinates and weights exactly. However, this approach necessitated a by far larger number of integration points than needed by the *Gauss-Legendre quadrature*.

3.3.1.3 Particle integration

Another possibility to become independent of a background grid is the particle integration. A major benefit of this integration scheme is that no computing time has to be invested in mesh generation and distribution of the integration points. Furthermore, when plotting the solution at the particles, the MLS shape functions and their derivatives have to be only calculated at particles, whereas in case of the Gauss quadrature also at the quadrature points. However, the particle integration usually causes oscillatory modes, because of under-integration and vanishing shape function derivatives at the particles.

Therefore, Beisel and Belytschko (1996) added to the problem functional a stabilization term which involved the second order derivatives of the shape functions. Nevertheless, it was stated that the particle arrangement was still a delicate matter in order to prevent spurious modes. Additionally, a hybrid formulation was proposed which should further stabilize the particle integration.

Chen and his co-workers (2001) made use of a *Voronoi diagram*, where the particles were placed in the center of each *Voronoi* cell. The strain at particles was then replaced by a divergence counterpart of its spatial average within each cell. By this, the resulting formulation did not involve shape function derivatives anymore and numerical instability due to vanishing shape function derivatives at particles was hoped to be cured. The computation of assumed particle strain needed the evaluation of the integral over the *Voronoi* cell boundary.

Randles et al. (1999) proposed to use another set of points additional to the existing the particle distribution. One set was used for the discretization of velocity and another set for stress and the velocity gradient. Thus, the derivatives of the approximants had not

to be computed at the particles which substantially reduced the oscillating behaviour and improved so the accuracy of the solution.

3.3.1.4 Summary

The majority of meshfree methods make use of the *Gauss-Legendre quadrature* which, however, involves the use of a background grid so that these methods can not be truly called meshfree. Furthermore, MLS-based meshfree methods are additionally subjected to integration errors due to the non-polynomial character of the shape functions and the misalignment between particle support zones and integration cells. Some researchers have tried to utilize a particle integration instead of *Gauss-Legendre quadrature*. However, spurious modes, due to vanishing shape function derivations and under-integration, are still an issue and need further investigations.

In this work a particle integration scheme is tested on the mixed variational formulation (Eq. 7.13) outlined in Sec. 7.2. As this formulation is enriched with second order derivatives of the displacement and stress fields, the vanishing first order shape function derivatives are hoped to be balanced out by the non-vanishing second order derivatives. However, the lacking approximation accuracy prevents in case of the *Gauss-Legendre quadrature* as well as the particle integration the use of this variational formulation for modelling purpose. For more details the reader is referred to Sec. 7.2. Therefore, the meshfree code which is part of this work solely relies on the *Gauss-Legendre quadrature* due to the lack of real alternatives.

3.3.2 Enforcement of essential boundary conditions

The enforcement of essential boundary conditions is surely the most critical issue in MLS-based meshfree methods. We recall that the MLS approximation functions (Eq. 3.5) do not meet the so-called *Kronecker Delta condition* $N_I(\boldsymbol{x}_J) \neq \delta_{IJ}$ which has as consequence that the particle parameters u_I in (Eq. 3.3) are not equal to the particles degrees of freedom, i.e. $u(\boldsymbol{x}_I) \neq u_I$. Therefore, the traditional boundary collocation method, which serves very well in FEM, can not be applied to MLS-based meshfree methods.

Now, there are basically four techniques to deal with the imposition of essential boundary conditions which will be addressed in the following.

3.3.2.1 Modified boundary collocation method

The *modified boundary collocation method* (Wagner and Liu 2000) was based on the traditional boundary collocation method, where the essential boundary conditions were exactly enforced only at the particles which are part of the boundary. In the following, a brief introduction on the traditional collocation method will help to illustrate its differences to the modified version.

Let a boundary value problem be defined on a domain $\Omega \in \mathbb{R}^3$ with boundary $\partial\Omega$

$$\mathcal{L}\mathbf{u}(\mathbf{x}) = \mathbf{f}(\mathbf{x}), \qquad \mathbf{x} \in \Omega \tag{3.45}$$

$$\mathbf{u}(\mathbf{x}) = \hat{\mathbf{u}}(\mathbf{x}), \qquad \mathbf{x} \in \partial\Omega_D, \tag{3.46}$$

where $\mathcal{L}$ is second order differential operator and $\partial\Omega_D \subset \partial\Omega$ denotes the Dirichlet boundary, where essential boundary conditions are applied. Eq. 3.45 is the so-called *strong form* of the boundary value problem. The multiplication with a weight function $\mathbf{w}(\mathbf{x})$ and partial integration leads to the so-called *weak form* of the problem

$$a(\mathbf{w}(\mathbf{x}), \mathbf{u}(\mathbf{x}))_{L_2(\Omega)} = (\mathbf{w}(\mathbf{x}), \mathbf{f}(\mathbf{x}))_{L_2(\Omega)}, \tag{3.47}$$

where $\mathbf{w}(\mathbf{x})$ is arbitrary in Ω and it is assumed

$$\mathbf{w}(\mathbf{x}) = \mathbf{0}, \qquad \mathbf{x} \in \partial\Omega. \tag{3.48}$$

Now let a particle distribution $\mathcal{D}$ be defined as follows

$$\mathcal{D} := \left\{ \mathbf{x}_I \,\middle|\, \mathbf{x}_I \in \Omega \right\}, \tag{3.49}$$

and $\Lambda \subset \mathcal{D}$ be the set of particles which support a point $\mathbf{x}$. Then the solution function $\mathbf{u}(\mathbf{x})$ and the weight function $\mathbf{w}(\mathbf{x})$ can be approximated with the help of a set of shape functions $\mathbf{N}_I(\mathbf{x})$ and corresponding particle degrees of freedoms $\mathbf{d}_I$ and $\mathbf{c}_I$, respectively

$$\mathbf{u}^h(\mathbf{x}) = \sum_{I \in \Lambda} \mathbf{N}_I(\mathbf{x})\, \mathbf{d}_I = \mathbf{N}(\mathbf{x})\, \mathbf{d} \tag{3.50}$$

$$\mathbf{w}^h(\mathbf{x}) = \sum_{I \in \Lambda} \mathbf{N}_I(\mathbf{x})\, \mathbf{c}_I = \mathbf{N}(\mathbf{x})\, \mathbf{c}. \tag{3.51}$$

In FEM, the traditional collocation method is usually applied on the weak form of the problem (Eq. 3.47) and the following expressions can be distinguished

$$\mathbf{c} \cdot \mathbf{r} = 0 \quad \text{(weighted residual vector)}, \tag{3.52}$$

$$\mathbf{r} = \mathbf{K}\mathbf{d} - \mathbf{f} \quad \text{(residual vector)}, \tag{3.53}$$

$$\mathbf{K} = a(\mathbf{N}(\mathbf{x}), \mathbf{N}(\mathbf{x})) \quad \text{(stiffness matrix)}, \tag{3.54}$$

$$\mathbf{f} = (\mathbf{N}(x), \mathbf{f}(\mathbf{x})) \quad \text{(force vector)}. \tag{3.55}$$

The elaborations outlined in the following consider the essential boundary conditions for each coordinate direction separately as they usually vary with the coordinate directions. Since the total number of particles n is the summation of the number of Dirichlet boundary particles $n_b \in \partial\Omega_D$ and the number of particles being placed on the Neumann boundary as well as in the interior domain $n_{nb} \in \tilde{\Omega} = \Omega \setminus \partial\Omega_D$

$$n = n_b + n_{nb}\,, \tag{3.56}$$

vectors $\mathbf{d}$, $\mathbf{c}$ and $\mathbf{r}$ are separated into two parts according to entries which are related to particles on $\partial\Omega_D$ and entries which correspond to particles in $\tilde{\Omega}$:

$$\mathbf{d} = \left\{ \begin{array}{c} \mathbf{d}_b \\ \mathbf{d}_{nb} \end{array} \right\}, \qquad \mathbf{c} = \left\{ \begin{array}{c} \mathbf{c}_b \\ \mathbf{c}_{nb} \end{array} \right\}, \qquad \mathbf{r} = \left\{ \begin{array}{c} \mathbf{r}_b \\ \mathbf{r}_{nb} \end{array} \right\}. \tag{3.57}$$

In a similar fashion the stiffness matrix $\mathbf{K}$, the force vector $\mathbf{f}$ and the shape function ordinates of the boundary particles $\mathbf{N}$ of all particles that support those boundary particles are modified

$$\mathbf{K} = \{\, \mathbf{K}_b\,,\, \mathbf{K}_{nb} \,\}\,, \qquad \mathbf{F} = \left\{ \begin{array}{c} \mathbf{F}_b \\ \mathbf{F}_{nb} \end{array} \right\}, \qquad \mathbf{N} = \{\, \mathbf{N}_b\,,\, \mathbf{N}_{nb} \,\}\,. \tag{3.58}$$

In order to enforce the essential boundary conditions we consider a vector $\mathbf{b}$ of size n_b with its elements defined by

$$b_I\left(\mathbf{x}_I\right) = \sum_{J \in \Lambda} N_J\left(\mathbf{x}_I\right) d_J - \hat{u}\left(\mathbf{x}_I\right) \tag{3.59}$$

and take into account that its elements need to be zero so that boundary conditions $u\left(\mathbf{x}_I\right) = \hat{u}\left(\mathbf{x}_I\right)$ at the corresponding boundary particles P_I are fulfilled. Now, all rows of the discrete equation system (Eq. 3.53) which are related to a boundary particle degree of freedom having an essential boundary condition applied are replaced by the corresponding elements of vector $\mathbf{b}$ and the weak form (Eq. 3.52) can be written as

$$\left\{ \begin{array}{c} \mathbf{c}_b \\ \mathbf{c}_{nb} \end{array} \right\} \cdot \left\{ \begin{array}{c} \mathbf{b} \\ \mathbf{r}_{nb} \end{array} \right\} = 0\,. \tag{3.60}$$

In FEM, it is furthermore admissible to modify the vectors which contain the particle degrees of freedom for the solution function $\mathbf{d}$ and the weight function $\mathbf{c}$ as follows

$$\mathbf{d} = \left\{ \begin{array}{c} \hat{\mathbf{u}} \\ \mathbf{d}_{nb} \end{array} \right\}, \qquad \mathbf{c} = \left\{ \begin{array}{c} \mathbf{0} \\ \mathbf{c}_{nb} \end{array} \right\}. \tag{3.61}$$

That is, the approximation of the solution function $u^h(\mathbf{x}_I)$ at boundary particles $P_I \in \partial\Omega_D$ equals the corresponding particle degrees of freedom d_I so that with Eq. 3.59 these degrees of freedom can be replaced with the corresponding essential boundary conditions. Recalling Eq. 3.48 the weight function is assumed to vanish at these boundary particles which is achieved by simply setting

$$\mathbf{c}_b = \mathbf{0}\,. \tag{3.62}$$

This simplification however, does not apply to MLS-based meshfree methods, because the approximation functions do not fulfill the *Kronecker Delta condition.*

In order to overcome this problem Wagner and Liu have modified the traditional collocation method which is described in the following. Let us recall the approximation of the weight function (Eq. 3.51) and write with (Eq. 3.57) an equation system which contains the approximation of the weight function at all particles $\mathbf{x}_I \in \Omega$

$$\begin{aligned}\left\{w^h(x_I)\right\} &= \left\{\begin{array}{c}\mathbf{w}_b^h\\ \mathbf{w}_{nb}^h\end{array}\right\} = \left\{\begin{array}{cc}\mathbf{N}_b(\mathbf{x}_I) & \mathbf{N}_{nb}(\mathbf{x}_I)\\ \mathbf{N}_b(\mathbf{x}_I) & \mathbf{N}_{nb}(\mathbf{x}_I)\end{array}\right\}\left\{\begin{array}{c}\mathbf{c}_b\\ \mathbf{c}_{nb}\end{array}\right\} = \\ &= \left\{\begin{array}{cc}\mathbf{A} & \mathbf{B}\\ \mathbf{C} & \mathbf{D}\end{array}\right\}\left\{\begin{array}{c}\mathbf{c}_b\\ \mathbf{c}_{nb}\end{array}\right\}, \quad I \in \Lambda\,.\end{aligned} \tag{3.63}$$

Now elements $\mathbf{w}_{nb}^h$ were replaced by the particle degrees of freedom $\mathbf{c}_{nb}$ which led to

$$\tilde{\mathbf{c}} = \left\{\begin{array}{c}\mathbf{w}_b\\ \mathbf{c}_{nb}\end{array}\right\} = \left\{\begin{array}{cc}\mathbf{A} & \mathbf{B}\\ \mathbf{0} & \mathbf{I}\end{array}\right\}\left\{\begin{array}{c}\mathbf{c}_b\\ \mathbf{c}_{nb}\end{array}\right\} = \tilde{\mathbf{N}}\mathbf{c}\,, \tag{3.64}$$

where $\mathbf{I}$ is the identity matrix of size $n_{nb} \times n_{nb}$. Now the weak form of our differential problem (Eq. 3.60) could be written as

$$\left\{\begin{array}{c}\tilde{\mathbf{c}}_b\\ \tilde{\mathbf{c}}_{nb}\end{array}\right\} \cdot \left\{\begin{array}{c}\left(\tilde{\mathbf{N}}^{-1}\right)^T\mathbf{b}\\ \left(\tilde{\mathbf{N}}^{-1}\right)^T\mathbf{r}_{nb}\end{array}\right\} = 0\,. \tag{3.65}$$

The inverse of $\tilde{\mathbf{N}}$ was expressed by

$$\tilde{\mathbf{N}}^{-1} = \left\{\begin{array}{cc}\mathbf{A}^{-1} & \mathbf{A}^{-1}\mathbf{B}\\ \mathbf{0} & \mathbf{1}\end{array}\right\}, \qquad \left(\tilde{\mathbf{N}}^{-1}\right)^T = \left\{\begin{array}{cc}\left(\mathbf{A}^{-1}\right)^T & \mathbf{0}\\ -\mathbf{B}^T\left(\mathbf{A}^{-1}\right)^T & \mathbf{1}\end{array}\right\}. \tag{3.66}$$

In the same way it was dealt with the approximation of the solution function $u^h(\mathbf{x})$

$$\tilde{\mathbf{d}} = \left\{\begin{array}{c}\mathbf{u}_b\\ \mathbf{d}_{nb}\end{array}\right\} = \left\{\begin{array}{cc}\mathbf{A} & \mathbf{B}\\ \mathbf{0} & \mathbf{1}\end{array}\right\}\left\{\begin{array}{c}\mathbf{d}_b\\ \mathbf{d}_{nb}\end{array}\right\} = \tilde{\mathbf{N}}\mathbf{d}\,. \tag{3.67}$$

and Eq. (3.65) was transferred to the following form

$$\left\{ \begin{array}{c} \tilde{\mathbf{c}}_b \\ \tilde{\mathbf{c}}_{nb} \end{array} \right\} \cdot \left\{ \begin{array}{c} \left(\tilde{\mathbf{N}}^{-1}\right)^T \mathbf{N}\tilde{\mathbf{N}}^{-1}\tilde{\mathbf{d}} - \hat{\mathbf{u}} \\ \left(\tilde{\mathbf{N}}^{-1}\right)^T \mathbf{K}\tilde{\mathbf{N}}^{-1}\tilde{\mathbf{d}} - \left(\tilde{\mathbf{N}}^{-1}\right)^T \mathbf{f} \end{array} \right\} = 0\,. \tag{3.68}$$

Similar to the traditional collocation method the modified particles degrees of freedom $\tilde{d}_I$ which correspond to boundary particles $P_I \in \Omega_D$ could be replaced by the corresponding essential boundary conditions and, assuming that the weight function $w^h(\mathbf{x})$ vanished on $\partial\Omega_D$, it held $\tilde{\mathbf{c}}_b = \mathbf{0}$. Consequently, Eq. (3.67) and Eq. (3.63) were modified as follows

$$\tilde{\mathbf{d}} = \left\{ \begin{array}{c} \hat{\mathbf{u}} \\ \tilde{\mathbf{d}}_{nb} \end{array} \right\}, \qquad \tilde{\mathbf{c}} = \left\{ \begin{array}{c} \mathbf{0} \\ \tilde{\mathbf{c}}_{nb} \end{array} \right\}. \tag{3.69}$$

The essential boundary conditions were enforced by incorporating the relations (Eq. 3.69) into the modified discrete equation system (Eq. 3.68). After solving this final modified discrete linear equation system the real particle parameter vector $\mathbf{d}$ could be finally determined by

$$\mathbf{d} = \tilde{\mathbf{N}}^{-1}\tilde{\mathbf{d}}\,. \tag{3.70}$$

Note that the entire algorithm must be applied for each coordinate direction separately.

The procedure appears to be very straightforward as the essential boundary conditions can be directly enforced, after the discrete equation system has been modified. However, the implementation is very involved. Firstly, in order to avoid large scale matrix multiplications those parts of the discrete equation system, which have to be modified, must be determined beforehand. This requires an elaborate algorithm as the boundary particles only interact with certain particles in their vicinity and correspondingly, the majority of the discrete equation system is not affected. Secondly, a sparse storage scheme is usually applied to the coefficient matrix so that only its band structure is considered. After the modification of the coefficient matrix some elements of the original matrix which happen to be zero become non-zero in the modified matrix. This fact must be taken into account, when the structure of the sparse storage scheme is initially ascertained.

Another issue is that during the transformation of the discrete equation system the original coefficient matrix and the modified one must be kept allocated at the same time. Thus, already medium size problems can exceed the memory limits of a single workstation. Furthermore, despite the fact that the boundary condition enforcement is precise at the boundary particles, it is not on the Dirichlet boundary as a whole. This is due to the characteristic of MLS-based meshfree methods that the boundary conditions are literally enforced only on the boundary particles, but not between them. In case of the Gauss quadrature however, the integration points are distributed between the boundary particles, where the boundary conditions are not exactly enforced. Whereas the finite element method

can fulfill constant essential boundary conditions exactly on the entire Dirichlet boundary, this is not the case for meshfree methods using the modified boundary collocation method. Especially for a curved boundary a sufficiently dense particle distribution on the boundary must be ensured in order to provide an accurate solution on the boundary and consequently for the whole domain.

This method is implemented in the meshfree code which is part of this research project. Despite its deficiencies the method was found to be numerically very stable.

3.3.2.2 Penalty method

Using the *penalty method* is probably the easiest way to impose the essential boundary conditions (Belytschko *et al.* 1994a; Liu and Chen 2001). It results in a banded and positive definite coefficient matrix of the discrete equation system. The boundary enforcement accuracy corresponds to the magnitude of the penalty parameter, which, accordingly, has to be set to a fairly high value. However, the solution is significantly dependent on the value of the penalty parameter considering that the penalizing physically represents the stiffness of fictional springs enforcing the constraints. If the essential boundary conditions affect large parts of boundary, the problem can become unsolvable as the penalty treatment basically replaces parts of the coefficient matrix of the discrete equation system by values of very high magnitude which are not related to the initial formulation which describes the physical state of the body under consideration. Particularly in MLS-based meshfree methods the affected parts of the coefficient matrix are much larger than in FEM due to the larger particle support.

3.3.2.3 Lagrange multiplier method

An alternative is the *Lagrange-multiplier-method* which introduces to the problem another unknown field the so-called *Lagrange multipliers* (Belytschko *et al.* 1994b; Chen *et al.* 1997; Ventura 2002). Even if the implementation of this method is not complicated and a very high boundary condition fulfillment accuracy can be achieved, it has to deal with two main disadvantages. Firstly, the problem size is increased as it contains a further unknown field and secondly, the coefficient matrix of the discrete equation system is neither positive definite nor banded. This procedure is therefore not suitable for larger problems. These drawbacks can be partly avoided, if the Lagrange multipliers can be identified with a physical quantity corresponding to constraint reaction resultant. This leads to a modified variational principle (Lu *et al.* 1994) which holds the benefit that the coefficient matrix of the discrete equations system is banded. However, the boundary enforcement accuracy is significantly less compared to the original Lagrange multiplier method. The authors mentioned that an increase of the particle distribution near to Dirichlet boundary could enhance the imposition of essential boundary conditions. Nevertheless, the presented examples only consider linear geometry and material, whereas non-linearity requires higher accuracy to achieve a reasonable convergence rate.

3.3.2.4 Stabilized modified variational principle

The lacking boundary enforcement accuracy of the kind of modified variational principle addressed in the previous section can be improved, if a penalty term is added (Nitsche 1970-1971). The stabilized modified variational principle holds the benefit that the coefficient matrix is not as much manipulated as in case of the penalty method, because the penalty term only serves for stabilizing purpose and so the magnitude of the penalty parameter can be set lower than in case of the penalty method. Nevertheless, the stabilization term ensures that the coefficient matrix is not ill-conditioned.

Related to this approach is the so-called *augmented Lagrangian method* (Hestens 1990; Powell 1969) which was initially proposed in order to improve the Lagrange multiplier method by avoiding an ill-conditioned discrete equation system and so ensuring a higher convergence rate.

In Sec. 4.1 a modified variational formulation is developed which is based on Nitsche's formulation. Note however, that Nitsche's formulation only considered linearity, whereas the approach derived in this thesis involves non-linearity in geometry and material. In fact, the non-linearities prove to be very significant in the application of the proposed method.

In Sec. 4.2 a new technique is proposed which allows to stabilize the modified variational principle introduced in the previous section in a flexible and adaptive way.

3.3.2.5 Hybrid FEM-meshfree method

Another possibility to impose the essential boundary conditions is to combine a MLS-based meshfree method and FEM in such a way that the domain boundary consists of a layer of finite elements and the interior domain of a meshfree particle distribution. As already mentioned in the paragraph on the traditional boundary collocation method, the boundary condition enforcement in FEM is easily achieved and the advantages of the meshfree approximation is maintained for the interior domain (Krongauz and Belytschko 1996).